Fluidic Innervation Sensorizes Structures from a Single Build Material

Ryan L. Truby, 1,2,†,* Lillian Chin, 1,† Annan Zhang, Daniela Rus 1

¹MIT Computer Science and Artificial Intelligence Lab, Massachusetts Institute of Technology, 32 Vassar St, Building 32, Cambridge, MA 02139, USA

²Departments of Materials Science and Engineering and Mechanical Engineering, Northwestern University, 2200 Campus Drive, Cook Hall, Evanston, IL 60208, USA

†These authors contributed equally.

*To whom correspondence should be addressed; E-mail: rtruby@northwestern.edu

Multifunctional materials with distributed sensing and programmed mechanical properties are required for myriad emerging technologies. However, current fabrication techniques constrain these materials' design and sensing capabilities. We address these needs with a method for sensorizing architected materials through fluidic innervation, where distributed networks of fluidic channels are directly embedded within an architected material's sparse geometry. This technique creates 3D printed, single-material structures that perceive deformations by measuring pressure changes within the fluidic sensors. With this strategy, we fabricate sensorized soft robotic actuators based on handed shearing auxetics and accurately predict their kinematics from the sensors' proprioceptive feedback using supervised learning. Our strategy for integrating structural, sensing, and actuation capabilities through control of form alone simplifies sensorized material design for applications spanning

wearables, smart structures, and robotics.

One-Sentence Summary: Through the fabrication of vascularized architected materials, we present a method for creating multifunctional structures that possess distributed sensing, actuation, and programmed mechanical behaviors through form alone.

Main Text

Multifunctionality is a defining feature in the composition and forms of biological systems (1,2). For example, the xylem of vascular plants participates in water and nutrient transport while directly contributing to structural integrity and resiliency (3). Likewise, the hierarchical structure of skeletal muscles facilitates the innervation and vascularization of densely packed muscle fibers, fulfilling the actuation, proprioception, and metabolic needs of vertebrate locomotion (4, 5). These materials and structures have evolved to address multiple needs in a single composite, enabling living organisms to efficiently achieve the performance required for their continued survival and evolutionary fitness. Inspired by these lessons, engineers have increasingly explored multifunctionality in materials design as a strategy to improve the performance, range of capabilities, and efficiency of a broad range of new technologies (2, 6).

In particular, a large subset of emerging technologies require multifunctional materials with programmable mechanical properties and distributed sensing (6-9). Recent works have demonstrated that bioinspired somatosensory materials can potentially address key performance challenges in next-generation smart structures (10-14), wearable devices (15-18), and robots (19-24). However, the materials used in these applications typically have strict mechanical requirements, such as high strength to weight ratios, extreme stiffness or compliance, and stretchability. These constraints make it difficult to imbue existing optimized materials with sensing. Indeed, current approaches to creating sensorized materials – and multifunctional

materials in general – involve the integration of multiple materials, either through manual assembly (10, 14, 16, 18, 19, 21-24), microfabrication (15, 17, 20), or specialized 3D printing methods (11-13). These fabrication techniques involve specialized, low-throughput, and/or complex methods or equipment that are often limited in the materials they can assemble. Their limitations prevent both the desired mechanical and sensory needs from being met optimally.

Motivated by these challenges, we present a strategy for fabricating multifunctional materials with programmable mechanical behaviors and distributed sensing capabilities by controlling the form of a single build material. Our strategy involves the sensorization of architected materials via open fluidic networks, which we construct via 3D printing (Fig. 1) (25). Architected materials are a class of materials that achieve tailorable mechanical properties entirely via geometry (26). While this makes them excellent for achieving optimally programmed mechanical performance, architected materials' dependence on geometry makes them difficult to sensorize. We surmount this problem by embedding fluidic networks directly into an architected material's internal structure. Once sealed, the networks' internal pressures can be measured as voltage signals during deformation and used as sensory feedback (27–29). This analog electronic feedback is distinct from other types of soft fluidic sensors that provide solely binary mechanical feedback (30, 31). Our methods present three key opportunities. First, fluidic innervation provides a straightforward route for placing, distributing, and fabricating sensors within the sparse geometries of architected materials. Second, our fluidic sensing strategy avoids the time-varying effects common to current soft material-based sensors. Soft sensors based on conductive liquids, piezoresistive elastomers, and viscoelastic waveguides are susceptible to drift and hysteresis due to their underlying microstructures and/or physicochemical behaviors (32). Our fluidic sensing strategy avoids these issues by embedding sensors directly within the structure. Finally, our methods enable the creation of soft robotic systems with true somatosensory capabilties. Building off our recent efforts to develop novel compliant materials for motorized

soft robots (33–36), we use our methods to sensorize a group of materials called handed shearing auxetics (HSAs) that our group has previously introduced (34). This combination of motors and fluidic sensing yields a soft robotic system with robust actuation and perception capabilities. Our system is not susceptible to failure by over-pressurization or leakage as is common in fluidically actuated soft robots, allowing us to operate the device for extensive periods of time. We collect large sensorimotor data sets and develop a deep neural network to propriop-ceptively predict the multi-degree-of-freedom actuator's kinematics. Fluidic innervation of the HSA's complex, sparse geometry represents a first embodiment of a multifunctional construct with integrated structural, sensing, and actuation capabilities achieved from one single building material.

We first demonstrate our approach by 3D printing sensorized versions of common lattice architectures (Fig. 1A). As outlined in Fig. 1B, lattices with distributed fluidic networks are 3D printed via digital light processing (DLP) from photopolymer resins. Non-polymerized resin trapped within the fluidic networks during the printing process is aspirated by vacuum (SI Video 1), and channels are flushed with solvent. After parts are completely cured, fluidic sensor networks are connected to differential pressure transducers via elastomeric tubing (Fig. 1C). While DLP affords the patterning resolution required to create our complex structures, the overall green-body strength and printing resin's viscosity and pot life limit the overall dimensions of fluidic features we can pattern. We investigate the fabricable sensor geometries for multiple printing resins and find that the dimensions of successfully fabricated fluidic networks are resin-dependent (Fig. S5, see *Materials and Methods*).

According to Boyle's law, deformation of the fluidically innervated materials results in changes of the internal pressure of the networks, P, inversely proportional to volume changes (i.e., decreases via compression, increases via extension). P is measured using the in-line differential pressure transducers, which report P-dependent voltages, V. We demonstrate these

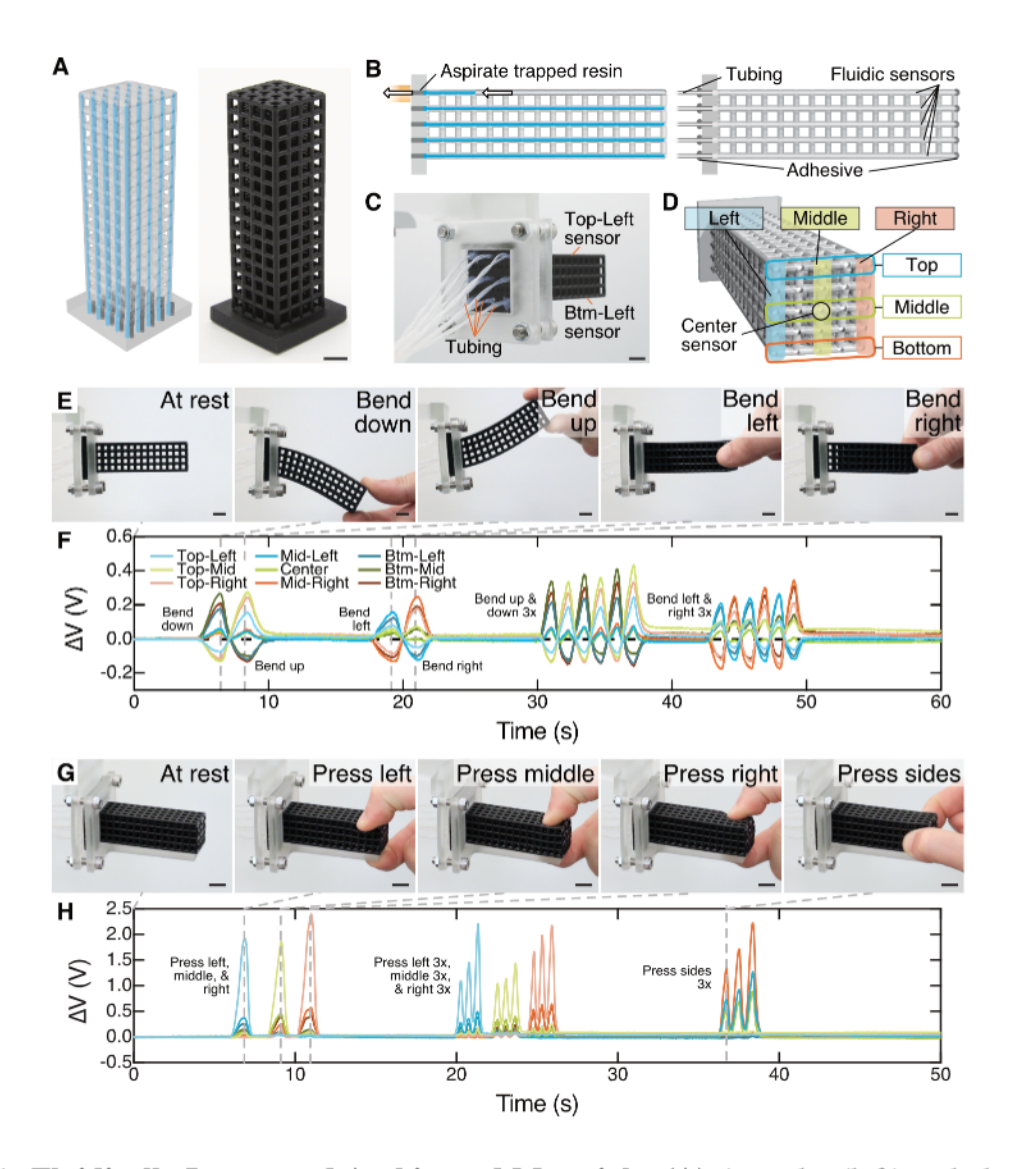


Figure 1: **Fluidically Innervated Architected Materials.** (A) A render (left) and photograph (right) of the sensorized cubic lattice. (B) Trapped resin (blue) is aspirated from the printed networks via vacuum (left), and tubing is inserted into fluidic sensors after final curing step. (C) The photograph shows the sensorized lattice from behind with tubing running from each sensor. (D) The schematic shows a sensor map for the nine sensors in the lattice. (E, G) Photographs from SI Video 2 with (F) the corresponding voltage change, ΔV , over time from all sensors during manual bending and (H) ΔV over time during tactile, pressing interactions. (Scale bars represent 1cm.)

operating principles in Fig. 1 using the simple cubic lattice printed from an elastomeric resin (EPU 40, Carbon). The lattice has nine straight fluidic sensors running along its length (see Fig. 1D). The "Top" and "Bottom" (Btm) sensors lie on the top and bottom row of struts in the beam, respectively. The "Middle" (Mid) sensors lie in the center row of struts, at the approximate neutral plane of the beam during downward and upward bending. "Left", "Middle" and "Right" sensors fall in the leftmost, middle, and rightmost columns of struts. Thus, left and right sensors lie on opposite sides of the neutral plane when the beam undergoes left- and rightward bends. As the cubic lattice undergoes manual bending (Figs. 1E-F, SI Video 2), we observe decreases in P for the sensors lying above the neutral plane ($\Delta V < 0$), while sensors below it report an increase in P ($\Delta V>0$). Notably, middle sensors lying in the neutral plane only produce a small voltage increase, likely due to compression by the solid struts parallel to the direction of bending. In Figs. 1G-H and SI Video 2, we explore tactile sensor response by pressing on individual columns of sensors. In all instances, we observe increases in P during compression ($\Delta V>0$), which are consistent with our results from manual bending. We also observe a depth-dependent response, with sensors closer to the contact point providing greater ΔV than those further from it. Importantly, in both sets of experiments, we observe clear, highly responsive feedback from all sensors during lattice deformation. Any instances where ΔV does not return to $\Delta V=0$ after deformation result from either the lack of precise motion in manual deformations and/or the intrinsic creep and stress relaxation of the proprietary viscoelastic resins (36). Over a 12-hour thermal drift study, we observed stable sensing (Fig. S7 and Supplementary Text). Figs. S8, S9 provide details of the data in Figs. 1E-H.

We quantitatively study fluidic sensing with elastomeric, fluidically innervated body-centered cubic (BCC) and octahedral lattices undergoing compression (Fig. 2). Figs. 2A,B show schematics of the BCC and octahedral lattices with five fluidic sensors of approximately equal volume. We selected BCC (M=-13) and octahedral lattices (M=0) for their similar ar-

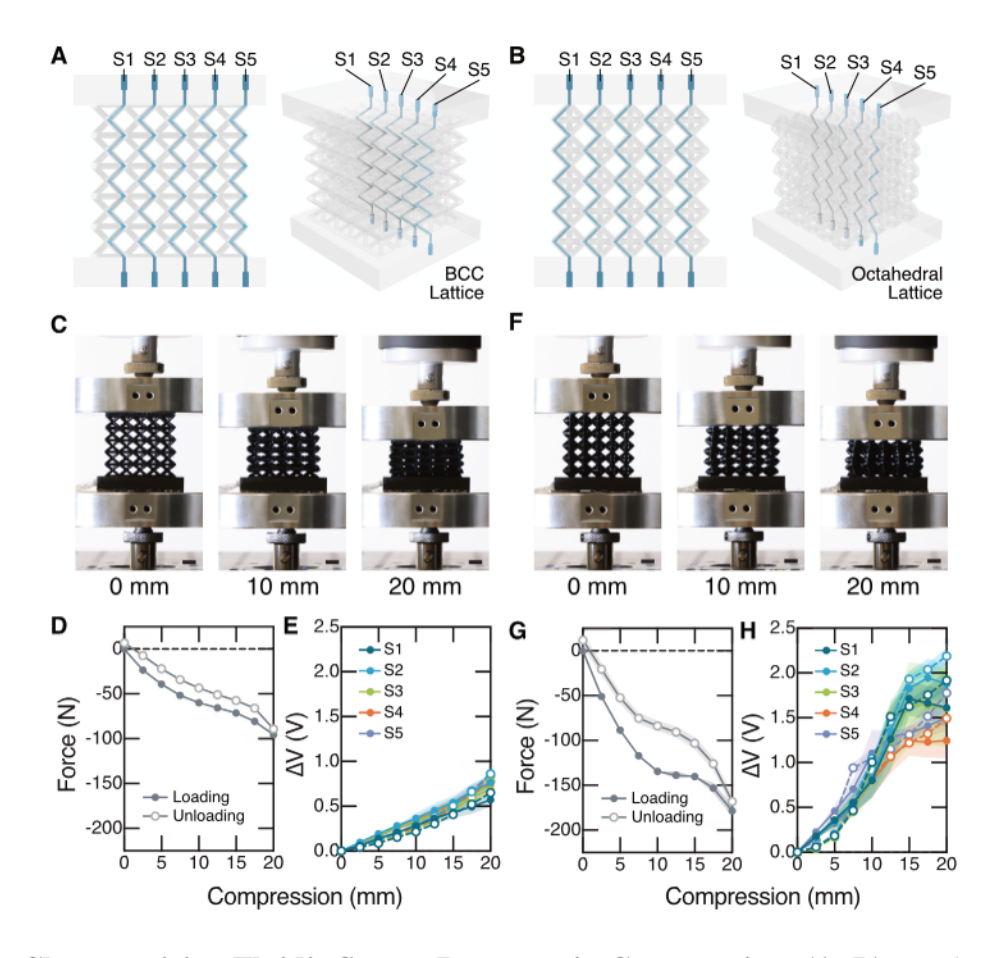


Figure 2: Characterizing Fluidic Sensor Response in Compression. (A, B) Renders of face-on (left) and perspective (right) views of (A) BCC and (B) octahedral lattices sensorized with five fluidic sensors centered within the structure. (C, F) Photographs from compression tests of sensorized BCC and octahedral lattices, respectively, with corresponding (D, G) force versus compression data and (E,H) voltage change, ΔV , versus compression response from all sensors. In C-H, data points and error bands represent mean and SD (n=3), and loading and unloading data are provided as filled and unfilled symbols, respectively. (Scale bars represent 1 cm.)

chitecture yet different bending- and stretching-dominated mechanical behaviors, respectively, according to Maxwell's stability criterion, M. During compression testing (Figs. 2C,F), we observe that the octahedral lattice is stiffer than the BCC lattice (Figs. 2D,G). This stiffness is reflected in the higher ΔV measured in the octahedral lattice's sensors (Figs. 2E,H), corresponding to higher forces required for compression. In these experiments, we observe that the five sensors in each lattice behave similarly for compressive forces below approximately 100 N. Data from cyclic compression experiments in Figs. S10 and S11 reveal that the viscoelasticity of the crosslinked resins is responsible for any time-varying behavior in the sensors. Even after 10,000 cycles of compression (Fig. S12), we observe largely non-hysteretic sensor responses given the fluidic sensing approach (Supplementary Text). These results suggest our sensorization technique is practical for architected structures and is a reliable alternative to soft matter-based conductors.

We next turn to the sensorization of HSAs, a new class of architected materials our group has developed for the design of motorized soft robots (34–36). Through a repeated joint linkage design, the HSA form tightly couples twisting with linear extension, enabling a single motor to drive a pair of HSAs as a compliant, soft robotic actuator. As with other architected materials, HSAs are difficult to sensorize due to their complex forms, and sensors must accommodate HSAs' extreme deformation (37). Sensorizing via fluidic innervation bypasses this issue by allowing us to embed sensors within the HSA architecture. Using a flexible polyurethane resin (FPU 50, Carbon) (36), we 3D printed two different sensorized HSAs (sHSAs), each with three embedded fluidic sensors. The first sHSA is based on a straight, unconstrained variety (Fig. 3A). The straight sHSAs' "Full," "Half," and "Quarter" sensors weave through the sHSA structure, terminating at 1x, 0.5x, and 0.25x the sHSA length. respectively. The second sHSA is based on a bending, constrained variety as shown in Fig. 3B. Adding constraint features in the HSA turns otherwise linear extension into out-of-plane bending (35). The bending sHSAs'

sensors are called "1/4", "3/4", and "1/2". We select these asymmetric sensor designs to sense different areas and modes of sHSA deformation.

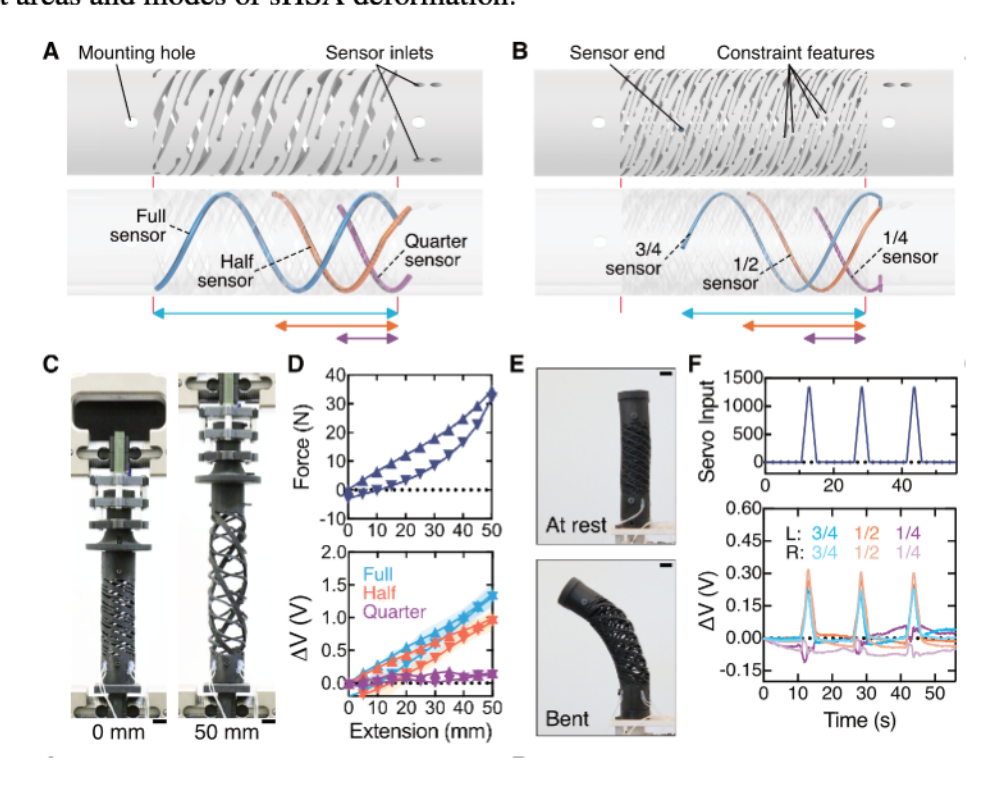


Figure 3: Sensorizing Electrically-Actuatable Handed Shearing Auxetics (HSAs). (A, B) Schematics of (A) straight and (B) bending sensorized HSAs (sHSAs) show the overall sHSA shape (top) and internal placement of the fluidic sensors (bottom). (C) The photographs show a straight sHSA at 0mm and 50mm extension. (D) Plots of extension force (top) and voltage change, ΔV , for the Full, Half, and Quarter Sensors (bottom) versus extension are provided for 1.5mm sensor diameters. Error bands represent standard deviation (n=3). Triangles pointing upwards and downwards represent data points during extension from 0 to 50mm and from 50 to 0mm, respectively. (E) Photographs of a soft robotic actuator comprised of two bending sHSAs of opposite handedness show at-rest and bent configurations. (F) Plots of servo input (top) and ΔV for the 3/4, 1/2, and 1/4 sensors in the L- and R-handed sHSAs (1mm sensor diameters, bottom) versus time are provided as the actuator under goes three actuation cycles. (Scale bars represent 1 cm.)

We characterized fluidic sensor responses embedded in straight sHSAs via cyclic tensile extension (Fig. 3C). sHSA extension yielded increasing ΔV for the Full and Half sensors (with 1.5mm diameters, Fig. 3D). As the sensors' diameters were increased, we observed increasing

sensitivity from the Full and Half sensors (Fig. S13). This is expected because larger sensor volumes provide larger pressure changes during identical deformations (Supplementary Text). Similarly, the Quarter sensor's small volume leads to negligible sensitivity during linear extension in all cases. Following an analogous investigation, we found that a sensor diameter of 1mm is appropriate for bending sHSAs given the reduced width of their widest struts (Fig. 3B). We then used two oppositely handed bending sHSAs and constructed the soft robotic finger shown in Fig. 3E and SI Video 3. While the sensors in this device have the smallest volume of any presented in this work, we see agreement between servo input and V for the 3/4 and 1/2 sensors in Fig. 3F. The small-volume 1/4 sensors report a noisy response, due to their placement giving either a low sensitivity to bending or a minimal deformation with respect to the locations of the rigid constraint features.

To demonstrate a sensorized version of an electrically-driven, sHSA-based soft robot, we constructed the system shown in Figs. 4A and S15. The design of this four degree-of-freedom (DOF) soft robotic platform was originally introduced in Reference (35) and is comprised here of four straight sHSAs with 1.5mm-diameter Full, Half, and Quarter sensors. Each sHSA is actuated by a different servo motor, with neighboring sHSAs having opposite handedness. Thus, the overall soft robot possesses 12 fluidic sensors and four servos for actuation. Figs. 4A-B and SI Video 4 show several of the maneuvers capable with the soft robot and the corresponding sensor responses, while Fig. S16 provides the corresponding servo inputs.

Despite an increasing focus on data-driven approaches for solving longstanding challenges in soft robot control (21, 23, 24, 38, 39), the robustness and reliability of current soft robotic actuation and sensing strategies limit the size of datasets that can be acquired for prioprioceptively determining shape or kinematics in soft sensorized robots. For example, popular pneumatically-actuated soft robots are notoriously susceptible to premature failure from over-pressurization with repeated actuation, making it challenging to build sufficiently large datasets. To evaluate

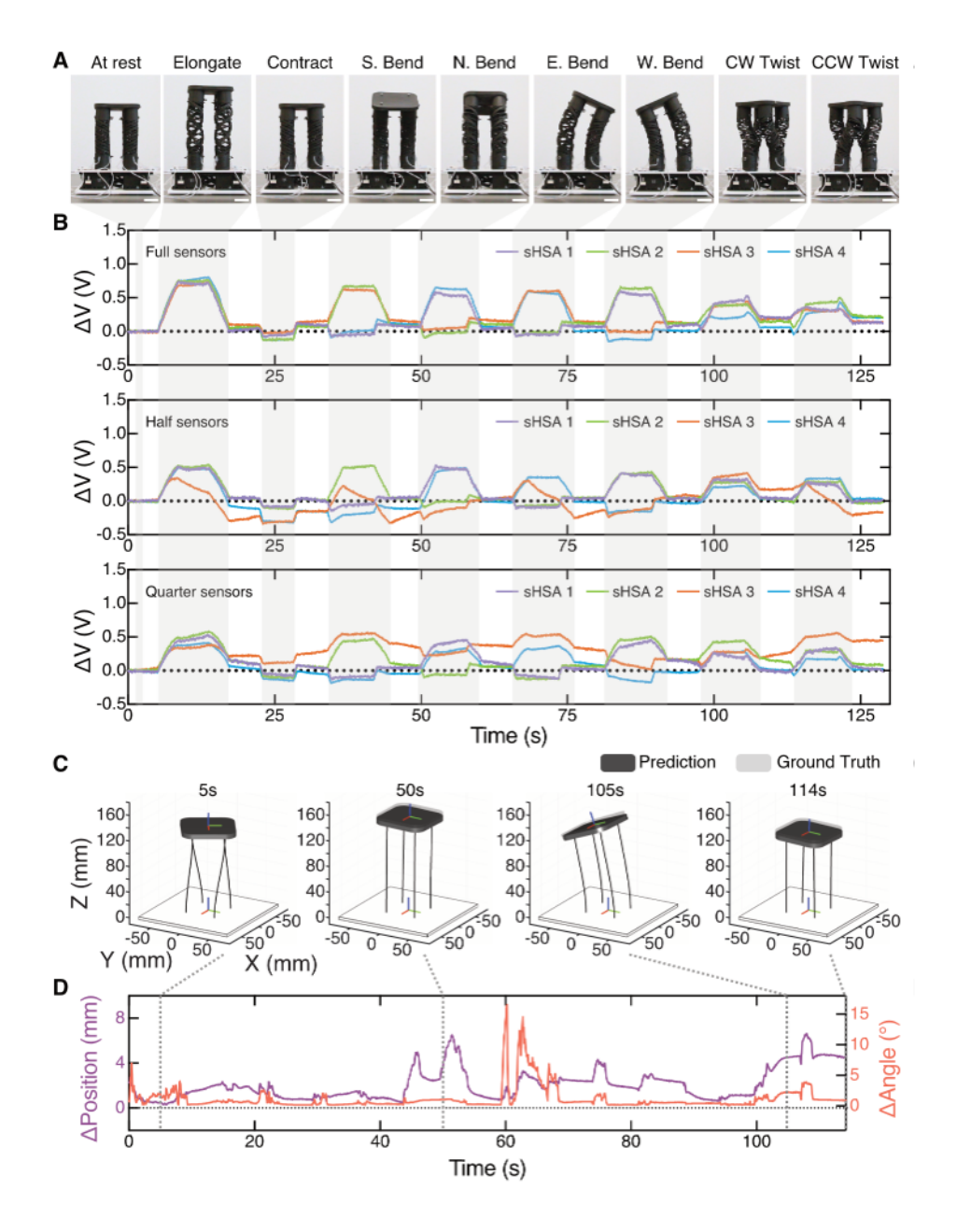


Figure 4: **Proprioception in an sHSA Platform** (A) Photographs of a sensorized HSA platform in motion and (B) corresponding changes in the voltage changes, ΔV , over time from the Full (top), Half (middle), and Quarter Sensors (bottom). (C) Snapshots from animations in SI Video 5 of the predicted and ground truth postures of the sHSA Platform are provided for an actuation sequence from our test set with (D) a corresponding plot of the position (Δ Position) and orientation (Δ Angle) error over time. The animation snapshots aid in visualizing the predicted and ground truth platform predictions at 5s, 50s, 105s, and 114s. (Scale bars represent 25mm.)

the robustness of our system in alleviating performance challenges in data-driven approaches to soft robotic perception, we drove our soft robot through varying extents of its 4 DOFs for over 18 hours of sensorimotor experimentation, measuring sensor responses against a motion capture ground truth. This long data collection period is notably large for a soft robotic system. As described in the Supplementary Text, we then used this large, rich dataset to train a longshort-term-memory (LSTM) based deep neural network capable of proprioceptively predicting the soft robot's kinematics based solely on the data from 12 fluidic sensors as model inputs (Fig. S18). Other data-driven sensing pipelines based on soft sensors with time-varying, hysteretic behaviors require neural networks with large numbers of hidden layers (21, 23). We achieve accurate pose predictions of our sHSA platform with just a relatively simple network. Figs. 4C-D and SI Video 5 show animated representations of our ground truth and model-predicted rigid-body pose of the platform with corresponding Euclidean distance (i.e., position) error and rotational angle error over the course of representative time series (see Fig. S20 for error explanation). While we certainly observe outlying instances, we generally observe that kinematic predictions align well with ground truth when soft robot motion is more continuous and holding of a pose is minimized. We suspect that this is due to the use of voltage changes as model inputs, as opposed to absolute voltage values. For interpreting the prediction data shown in Figs. 4C,D and SI Video 5, we note that the rest length of the sHSA platform is 120 mm, and the maximum vertical extension is approximately 40 mm. The overall position error in Fig. 4D is small compared to these lengths. Thus, our motorized sHSAs and fluidic sensing strategies allow us to bring robust actuation and perception capabilities to soft robotics, bypassing both of these problematic issues for the field.

In summary, we have demonstrated the versatility and integrity of our fluidic sensing strategy across a wide range of passive and active architected materials. Using a DLP-based printing method, we simultaneously create sensorized, architected materials and innervating vascular networks for fluidic sensing, bypassing the need for co-patterning structural materials with conductive materials that have extreme time-varying behaviors. Importantly, following a bioinspired approach to multifunctional material design, our approach to sensorizing structures through fluidic innervation greatly simplifies how materials with self-sensing and programmed mechanical behaviors can be fabricated. Through the sensorization of HSAs, we also introduce a soft robotic system representing a first demonstration of how a single build material can be architected to simultaneously achieve tailored structural properties, distributed sensing, and actuation capabilities. Coupling the simplicity of our sensorization approach with other digitally fabricated materials could herald fundamentally new opportunities for the design and manufacturing of sensorized materials for wearable devices, smart structures, autonomous bioinspired robots, and beyond.

References

- 1. U. G. K. Wegst, H. Bai, E. Saiz, A. P. Tomsia, R. O. Ritchie, Bioinspired structural materials. *Nature Materials* **14**, 23-36 (2015).
- 2. M. Eder, S. Amini, P. Fratzl, Biological composites—complex structures for functional diversity. *Science* **362**, 543-547 (2018).
- 3. L. J. Gibson, The hierarchical structure and mechanics of plant materials. *Journal of The Royal Society Interface* **9**, 2749-2766 (2012).
- 4. W. R. Frontera, J. Ochala, Skeletal muscle: A brief review of structure and function. *Calcified Tissue International* **96**, 183-195 (2015).
- 5. J. C. Tuthill, E. Azim, Proprioception. Current Biology 28, R194-R203 (2018).

- M. A. McEvoy, N. Correll, Materials that couple sensing, actuation, computation, and communication. *Science* 347, 1261689 (2015).
- G.-Z. Yang, J. Bellingham, P. E. Dupont, P. Fischer, L. Floridi, R. Full, N. Jacobstein, V. Kumar, M. McNutt, R. Merrifield, B. J. Nelson, B. Scassellati, M. Taddeo, R. Taylor, M. Veloso, Z. L. Wang, R. Wood, The grand challenges of science robotics. *Science Robotics* 3, eaar7650 (2018).
- 8. C. Kaspar, B. J. Ravoo, W. G. van der Wiel, S. V. Wegner, W. H. P. Pernice, The rise of intelligent matter. *Nature* **594**, 345–355 (2021).
- 9. M. Kaur, T.-H. Kim, W. S. Kim, New frontiers in 3d structural sensing robots. *Advanced Materials* **33**, 2002534 (2021).
- N. C. Sears, J. D. Berrigan, P. R. Buskohl, R. L. Harne, Flexible hybrid electronic material systems with programmable strain sensing architectures. *Advanced Engineering Materials* 20, 1800499 (2018).
- 11. Y. Yang, X. Li, M. Chu, H. Sun, J. Jin, K. Yu, Q. Wang, Q. Zhou, Y. Chen, Electrically assisted 3d printing of nacre-inspired structures with self-sensing capability. *Science Advances* 5, eaau9490 (2019).
- R. Hensleigh, H. Cui, Z. Xu, J. Massman, D. Yao, J. Berrigan, X. Zheng, Charge-programmed three-dimensional printing for multi-material electronic devices. *Nature Electronics* 3, 216-224 (2020).
- J. Gong, O. Seow, C. Honnet, J. Forman, S. Mueller, *MetaSense: Integrating Sensing Capabilities into Mechanical Metamaterial* (Association for Computing Machinery, New York, NY, USA, 2021), p. 1063–1073.

- 14. C. El Helou, P. R. Buskohl, C. E. Tabor, R. L. Harne, Digital logic gates in soft, conductive mechanical metamaterials. *Nat. Commun.* **12**, 1633 (2021).
- D. Son, J. Lee, S. Qiao, R. Ghaffari, J. Kim, J. E. Lee, C. Song, S. J. Kim, D. J. Lee, S. W. Jun, S. Yang, M. Park, J. Shin, K. Do, M. Lee, K. Kang, C. S. Hwang, N. Lu, T. Hyeon, D.-H. Kim, Multifunctional wearable devices for diagnosis and therapy of movement disorders. *Nature Nanotechnology* 9, 397-404 (2014).
- 16. H. Zhao, K. O'Brien, S. Li, R. F. Shepherd, Optoelectronically innervated soft prosthetic hand via stretchable optical waveguides. *Science Robotics* 1, eaai7529 (2016).
- M. Rein, V. D. Favrod, C. Hou, T. Khudiyev, A. Stolyarov, J. Cox, C.-C. Chung, C. Chhav,
 M. Ellis, J. Joannopoulos, Y. Fink, Diode fibres for fabric-based optical communications.
 Nature 560, 214-218 (2018).
- 18. H. Bai, S. Li, J. Barreiros, Y. Tu, C. R. Pollock, R. F. Shepherd, Stretchable distributed fiber-optic sensors. *Science* **370**, 848-852 (2020).
- C. Larson, B. Peele, S. Li, S. Robinson, M. Totaro, L. Beccai, B. Mazzolai, R. Shepherd, Highly stretchable electroluminescent skin for optical signaling and tactile sensing. *Science* 351, 1071-1074 (2016).
- R. L. Truby, M. Wehner, A. K. Grosskopf, D. M. Vogt, S. G. M. Uzel, R. J. Wood, J. A. Lewis, Soft somatosensitive actuators via embedded 3d printing. *Advanced Materials* 30, 1706383 (2018).
- 21. T. G. Thuruthel, B. Shih, C. Laschi, M. T. Tolley, Soft robot perception using embedded soft sensors and recurrent neural networks. *Science Robotics* 4, eaav1488 (2019).

- P. A. Xu, A. K. Mishra, H. Bai, C. A. Aubin, L. Zullo, R. F. Shepherd, Optical lace for synthetic afferent neural networks. *Science Robotics* 4, eaaw6304 (2019).
- R. L. Truby, C. D. Santina, D. Rus, Distributed proprioception of 3d configuration in soft, sensorized robots via deep learning. *IEEE Robotics and Automation Letters* 5, 3299-3306 (2020).
- 24. S. A. Manzano, P. Xu, K. Ly, R. Shepherd, N. Correll, High-bandwidth nonlinear control for soft actuators with recursive network models (2021).
- J. R. Tumbleston, D. Shirvanyants, N. Ermoshkin, R. Janusziewicz, A. R. Johnson,
 D. Kelly, K. Chen, R. Pinschmidt, J. P. Rolland, A. Ermoshkin, E. T. Samulski, J. M.
 DeSimone, Continuous liquid interface production of 3d objects. *Science* 347, 1349-1352 (2015).
- K. Bertoldi, V. Vitelli, J. Christensen, M. van Hecke, Flexible mechanical metamaterials.
 Nature Reviews Materials 2, 17066 (2017).
- J. Kim, A. Alspach, K. Yamane, 2015 IEEE/RSJ International Conference on Intelligent Robots and Systems (IROS) (2015), pp. 2419–2425.
- L. He, Q. Lu, S.-A. Abad, N. Rojas, T. Nanayakkara, Soft fingertips with tactile sensing and active deformation for robust grasping of delicate objects. *IEEE Robotics and Automation Letters* 5, 2714-2721 (2020).
- A. M. Gruebele, M. A. Lin, D. Brouwer, S. Yuan, A. C. Zerbe, M. R. Cutkosky, A stretchable tactile sleeve for reaching into cluttered spaces. *IEEE Robotics and Automation Letters* 6, 5308-5315 (2021).

- P. Rothemund, A. Ainla, L. Belding, D. J. Preston, S. Kurihara, Z. Suo, G. M. Whitesides, A soft, bistable valve for autonomous control of soft actuators. *Science Robotics* 3, eaar7986 (2018).
- 31. D. Drotman, S. Jadhav, D. Sharp, C. Chan, M. T. Tolley, Electronics-free pneumatic circuits for controlling soft-legged robots. *Science Robotics* **6**, eaay2627 (2021).
- S. Li, H. Bai, R. F. Shepherd, H. Zhao, Bio-inspired design and additive manufacturing of soft materials, machines, robots, and haptic interfaces. *Angewandte Chemie International Edition* 58, 11182-11204 (2019).
- 33. R. MacCurdy, R. Katzschmann, Y. Kim, D. Rus (2016), pp. 3878–3885.
- 34. J. I. Lipton, R. MacCurdy, Z. Manchester, L. Chin, D. Cellucci, D. Rus, Handedness in shearing auxetics creates rigid and compliant structures. *Science* **360**, 632–635 (2018).
- 35. L. Chin, J. Lipton, R. MacCurdy, J. Romanishin, C. Sharma, D. Rus (IEEE, 2018), pp. 100–107.
- 36. R. L. Truby, L. Chin, D. Rus, A recipe for electrically-driven soft robots via 3d printed handed shearing auxetics. *IEEE Robotics and Automation Letters* **6**, 795–802 (2021).
- 37. L. Chin, M. C. Yuen, J. Lipton, L. H. Trueba, R. Kramer-Bottiglio, D. Rus, 2019 International Conference on Robotics and Automation (ICRA) (IEEE, 2019), pp. 2765–2771.
- 38. R. K. Mehta, A. P. Sabelhaus, C. Majidi, Learned dynamics of electrothermally-actuated soft robot limbs using 1stm neural networks (2021).
- 39. K. Chin, T. Hellebrekers, C. Majidi, Machine learning for soft robotic sensing and control. Advanced Intelligent Systems 2, 1900171 (2020).

40. A. Géron, Hands-on machine learning with Scikit-Learn, Keras, and TensorFlow: Concepts, tools, and techniques to build intelligent systems (O'Reilly Media, 2019).

Acknowledgments

The authors would like to thank Dr. R. Hasani (MIT) for valuable discussions around data augmentation techniques for LSTM training. Funding: R.L.T. was supported by the Schmidt Science Fellows program, in partnership with the Rhodes Trust. L.C. was supported by the National Science Foundation (NSF) Graduate Research Fellowship under Grant #1122374, and the Fannie and John Hertz Foundation. This work was supported through the NSF EFRI Program under Grant #1830901. Author Contributions: Conceptualization: R.L.T., L.C.; Methodology: R.L.T., L.C., A.Z.; Software: R.L.T., L.C., A.Z.; Validation: R.L.T., L.C., A.Z.; Formal analysis: R.L.T., A.Z.; Investigation: R.L.T., L.C., A.Z.; Data Curation: R.L.T., L.C., A.Z.; Writing – Original Draft: all authors; Writing – Review & Editing: all authors; Supervision: R.L.T., D.R.; Funding Acquisition: D.R. Competing Interests: The authors have filed a provisional patent application related to this work. Data and Materials Availability: All data is available in the manuscript or supplementary materials. AZ: Add link to data RLT: Lilly, if I remember correctly, you are going to help Annan with this.

Supplementary materials

LTC: Edit this in the Word version to actually match what we put into SI. Also verify all references in text are right ("SI" or "Supple-

mentary Text")

Materials and Methods

Supplementary Text

Figs. S1 to S3

Tables S1 to S4

References (4-10)

Materials and Methods

3D Printing Fluidically Innervated Architected Materials. Fluidically innervated architected materials are parametrically designed in Rhino 6 and Grasshopper (Robert McNeel & Associates) with the Shortest Walk and Crystallon Grasshopper plug-ins. All parts are 3D printed via digital light processing (Carbon M1 printer, Carbon, Inc.) from commercially available elastomeric polyurethane (EPU 40), flexible polyurethane (FPU 50), and transparent resin Loctite 3D IND405 (LOCTITE) photopolymer resins (all from Carbon, Inc.). The sensorized lattices and handed shearing auxetics (sHSAs) are printed from EPU and FPU, respectively. All transparent models are printed from Loctite 3D IND405. The resins and printed structures are used and post-processed, respectively, according to the manufacturer's protocols. Supports are printed for sHSAs only.

The fluidic networks must be emptied and cleared of residual resin to prevent occlusion of the sensors before any UV- or thermal-curing steps are taken in the post-processing procedures. Upon removal of the part from the build platform, fluidic sensor networks are aspirated by vacuum. We use a vacuum to aspirate any remaining resin from printed fluidic networks because positive pressure can rupture the fluidic channels in the green body state. The channels are flushed with pressurized air, and isopropanol (IPA) is flushed into the inlet of each sensor for 5-15 sec to verify that the channel is open. Channels are flushed a second time with pressurized air and IPA. Parts are dried with pressurized air and post-processed according to the manufacturer's specifications.

Sensorization and Read-out Electronics. Sensor networks are designed with an inlet and an outlet, where inlets are locations for sensor tubing and outlets are included to facilitate removal of residual resin. After post-processing, silicone tubing (OD of 0.94 mm, ID of 0.51 mm, McMaster Carr) is glued into each sensor inlet using Silpoxy (Smooth-on). Pressurized air is

used to verify successful leak-proof adhesion of the tubing to the sHSA, and sensor outlets are closed by filling with a small amount of Silpoxy, creating a closed volume. Sensor tubing is then joined to differential pressure sensors by threading the sensor tubing into larger diameter tubing placed over the sensors' ports. Three differential pressure sensors (Amphenol, All Sensors) are used to measure pressure changes in the ranges of 0-0.5 in H_20 (0.5INCH-D1-4V-MINI), 0-1 in H_20 (1 INCH-D1-P4V-MINI), and 0-5 in H_20 (5 INCH-D1-P4V-MINI). 0-5 in H_20 differential pressure sensors are used for the fluidically innervated cubic, BCC, and octahedral lattices. 0-1 in H_20 pressure sensors are used for the Full and Half sensors of straight sHSAs, and the 3/4 and 1/2 sensors of the bending sHSAs. 0-0.05 in H_20 pressure sensors are used for the Quarter and 1/4 sensors of the straight and bending sHSAs, respectively. All output voltage signals from differential pressure sensors are filtered by a low-pass filter (cut-off frequency of \sim 30 Hz) and read by a digital acquisition unit (NI USB-6212 DAQ, National Instrutments).

The differential pressure sensors have two ports. The nominal voltage at a zero differential pressure (i.e., when both ports are at atmospheric pressure) is 2.25 V (Specification Sheet, Miniature Amplified Low Pressure Sensors, All Sensors). Therefore, one can select which port is connected to the fluidic sensor to achieve an increasing/decreasing voltage change with respect to 2.25 V for an increasing pressure in the fluidic sensor. As discussed in greater detail in the *Supplementary Text*, we mitigate effects due to thermal drift by connecting the second port of the differential pressure sensor to a dummy line, which comprises of identical silicone tubing that wraps around the tubing to the functional fluidic sensor. After all tubing is sealed and connected to the differential pressure sensor, we allow the sensors to reach equilibrium internal pressures for 48 hr, which is the timepoint on which a differential pressure sensor connected to a fluidic network reports a nominal voltage of approximately 2.25 V.

Print Parameter Characterization. The pressure drop, ΔP , required to remove all remaining resin via vacuum is dependent on the length, L, and radius, R, of the network, per the Hagen-Poiseuille equation,

$$\Delta P = \frac{8\mu L}{\pi R^4} Q \tag{1}$$

where μ is resin viscosity and Q is the flow rate initiated by the vacuum. To evaluate the fabricability of fluidic networks in architected materials, cubic lattices innervated with straight fluidic channels are printed as model structures with which print parameters can be screened. The lattices have a unit cell size of 5 mm, width of 5 cells, length of 5 cells, and a strut diameter of 2 mm. Within each lattice, there are 21 straight fluidic channels that span the height of the lattice, corresponding to three replicates of seven different channel diameters (i.e., 2R): 0.5, 0.75, 1.0, 1.25, 1.5, 1.75, and 2.0 mm. Six different heights (i.e., L) are evaluated: 5, 10, 25, 50, 75, and 100 mm. Pressurized air is flushed through each channel, which are noted as successful if air flows through freely and failed if air flow is blocked by incomplete removal of resin.

Characterization of Sensorized Lattices. Nine sensor responses in the cubic lattices are characterized by manual deformation in directional bending and pressing motifs. Five sensor responses from BCC and octahedral lattices are characterized using an Instron during cyclic, uniaxial compression. The BCC and Octahedral lattices' fluidic sensors have approximately equal volume and are positioned vertically within one central row of unit cells. Sensors from all sensorized lattices are measured at a sampling frequency of 50 Hz in all characterization experiments.

BCC and Octahedral lattices undergo at two rounds of break-in compression cycles before further characterization: 100 cycles of compression to 10mm at 1 mm/s and 100 cycles of

compression to 20mm at 5 mm/s. After break-in, the BCC and Octahedral lattices are then compressed at 2.5mm increments from 0 to 20 mm and then decompressed from 20 to 0 mm. At each (de)compression interval, a force measurement is recorded from the Instron, and the sensor readings are recorded for 10s, over which a mean and standard deviation output voltage is determined for each sensor. This process is repeated three times.

Lastly, the BCC lattice was cyclically compressed 10,000 cycles to 10mm at 1mm/s. For this study, sensor readings were recorded at 5 Hz.

Characterization of sHSAs. Sensor responses from straight sHSAs are characterized using an Instron during cyclic, uniaxial extension. Straight sHSAs with fluidic sensor diameters of 0.75, 1, 1.25, 1.5, and 1.75 mm were studied. Custom adapters are used to mount the straight sHSAs to the Instron to allow for free rotation of one end of the sHSA while fixing the other. Straight sHSAs are stretched in 5mm increments from 0 to 50 mm and then back to 0mm, with sensor readings recorded from each sensor by measuring the mean and standard deviation of the reading over 10 seconds of sampling at 50 Hz. Experiments are repeated three times. Before all experiments, straight sHSAs are cyclically extended 50mm at 10 mm/s for 100 cycles as break-in to remove any strain-softening behaviors due to the Mullins effect. sHSAs are then cycled at 1 mm/s for 10 cycles to validate no leaks are present.

Bending sHSA assemblies are actuated by Dynamixel MX-28 Servos (ROBOTIS) and controlled via MATLAB (Mathworks). Two sHSAs, each of opposite handedness, are counterrotated against each other in a geared setup with a single servo. Sensor readings are collected at \sim 15 Hz.

sHSA Soft Robotic Platform. Soft robotic fingers and multi-DOF platforms are constructed (as previously described in (36)) from sHSAs. Briefly, sHSA fingers and platforms are based on 2x1 and 2x2 assemblies of sHSAs with opposite handedness, respectively. Fingers are driven by

one servo motor, while platforms are driven by four (i.e., one servo per sHSA). All soft robotic systems are actuated by Dynamixel MX-28 Servos (ROBOTIS) and controlled via MATLAB (Mathworks).

Data Collection with sHSA Platform. Data for neural network prediction of the sHSA platform's pose was taken by driving the platform through a series of motions while simultaneously recording sensor values against a motion capture ground truth. For all experiments, the sHSA platform is actuated through a sequence of motions, returning to its neutral position after each one. The motions are: extension, compression, bend left, bend right, bend forward, bend backward, clockwise twist, and counter clockwise twist. For each trial, all of the motions are performed, but the order in which they are performed is randomized.

During these experiments, output voltage signals from differential pressure sensors are recorded by a digital acquisition unit (NI USB-6212 DAQ, National Instrutments) through MATLAB (Mathworks). MATLAB also directly records servo position feedback from the Dynamixel MX-28 servos (ROBOTIS). Ground truth readings are recorded through rigid body motion tracking via Motive (Optitrack). Data across software is synchronized via the interpolation of UNIX timestamps associated with each measurement, resulting in a final sampling frequency of 15 Hz. To normalize across trials, the initial sensor measurement for each trial is recorded as 0 V, so further sensor readings are reported as the pressure difference in the fluidic sensors.

To add variance across trials, a specific servo velocity, extent of motion range, and end-of-movement hold time are chosen from a pre-selected list of options. This causes each trial to be of different lengths, making it harder for the neural network to track spurious patterns. For example, a faster servo velocity will result in the sequence being completed in less time. The servo speeds studied were 5, 10, 20, and 40 rev / min. The hold times studied were 0, 5, and 10

seconds. The range fractions studied were 25%, 50%, 75% and 100% of full DOF range. For each given velocity, range and hold time, 5 trials were conducted.

In summary, 240 trials were autonomously recorded over a single 7 hour period. 19 of these trials did not have accurate synchronization between the motion capture and MATLAB recordings and were omitted. 9 more of these trials were found to have errors in the data concatenation process and were omitted as well. These experiments formed the dataset used for the neural network training, testing and validation. 11 hours of additional experiments were conducted to debug the data collection script, to break in and calibrate the sHSAs, and to take videos and photographs. RLT: I will check the 11 hour mark.

Neural Network Design, Training, and Testing. Learning Problem: To estimate the forward kinematics of the four-DOF sHSA platform, a neural network that predicts its pose (i.e., position and orientation) solely using analog voltage readings from the fluidic sensors as input is developed. Since time-dependent effects like stress relaxation and creep are inherent to viscoelastic materials used for the HSAs, the input-output relation is modeled with long-short-term-memory networks (LSTMs), a class of neural networks commonly used for learning-based proprioception in soft robotics because of their ability to capture temporal relations (21, 23, 24, 38).

Data Preprocessing: Out of the 212 remaining time sequences, the last 32 are set aside as the test set. Since this test data is neither used for model training nor for model selection, evaluating the final LSTM on it provides an unbiased estimate of the system performance in deployment. The data from the remaining 180 experiments account for $\approx 85\%$ of the total data and form the basis for the training and validation sets. Since the longest of these recordings consists of 3688 time steps, which is difficult to learn even for LSTMs, sequences of a more manageable length are extracted by sliding a window of length 64 over each recording (Fig.

S17). To simultaneously augment the data set, the window is slid with a stride of 20. The first data point in each recording (zero voltage difference for input data; initial pose for output data) is duplicated until the length of the recording equals 64 plus a multiple of 20. In this way, a total of 14,528 sequences with length 64 are generated. 1,453 ($\approx 10\%$) are split off randomly as a validation set to evaluate a particular choice of hyperparameters during the model selection process. Finally, training and validation sets are shuffled, inputs are normalized to zero mean and unit variance, and outputs are normalized to zero mean.

Neural Network Architecture: The neural network reads in a time sequence of 12-dimensional vectors (sensor voltages) and outputs a time sequence of 7-dimensional vectors (platform pose) with equal length (Fig S18). The inputs are first passed through stacked LSTM layers, where the number of layers and the number of hidden and cell states are tunable hyperparameters. The output of the LSTM layers are then passed through a fully-connected layer with equal input- and output-dimension, followed by ReLU (rectified linear unit) activation. The data is passed through another fully-connected layer that outputs a 7-dimensional vector. Finally, a normalization layer is applied to the four values corresponding to the orientation prediction, since an orientation is given by a 4-dimensional vector that represents the coefficients of a unit quaternion. To mitigate overfitting, the first fully-connected layer and all LSTM layers are equipped with a dropout probability of 0.2.

Since the coefficients of unit quaternions can be interpreted as points on a 4-dimensional hypersphere, the distance between two quaternions are described by the geodesic distance on the hypersphere. Furthermore, by definition of quaternions, antipodal points on the hypersphere describe the same orientation in 3-dimensional Euclidean space. However, the simple mean squared error (MSE) is found to be sufficient in practice, even though it neglects both the curvature of the hypersphere and the symmetry of quaternions. This choice is reasonable as long as training converges, since the Euclidean distance approximates the geodesic distance

for quaternions close to each other. The loss between predicted and ground truth pose is therefore computed as the sum of the position-MSE and the quaternion-MSE, though additionally weighted by a hyperparameter that balances the relative importance of minimizing these errors.

Model Selection: Starting around an initial configuration found by following best practice guidelines for training LSTMs (40), a grid search over the following hyperparameters is performed: quaternion weight (10, 100, 1000), initial learning rate (0.001, 0.005, 0.01), number of LSTM layers (1, 2, 3), and number of hidden and cell states (50, 100, 150, 200). Implemented in PyTorch, all models are trained with the Adam optimizer and a batch size of 32 for 100 epochs. The learning rate scheduler halves the learning rate when the validation error does not improve for 20 epochs. To avoid overfitting, an early stopping rule observing the loss on the validation set is employed. In other words, while training with a particular choice of hyperparameters, only the model that shows the lowest validation error across all 100 epochs is retained. To account for randomness during neural network training, the validation loss for a particular choice of hyperparameters is averaged over a total of three runs. Finally, the model with the lowest validation error across all possible choices of hyperparameters is retrained for 1000 epochs. Out of three runs, the run with the lowest validation loss is kept as the best model for evaluation on the test set. Summary statistics of this hyperparameter search can be found in Tab. S1 and Fig. S19.

Supplementary Text

Thermal Drift. Like most sensors, our fluidic sensors are susceptible to thermal drift. The ideal gas law informs us that our sensors' output voltages – which are dependent on pressure, P, within the fluidic sensor – are also dependent on temperature, T:

$$Pv = nRT (2)$$

where v is the fluidic sensor volume, n is the moles of gas within the sensor, and R is the ideal gas constant. Moreover, we also observe that our sensors are n-dependent as well. Our gaspermeable resins and the elastomeric tubing used to connect the fluidic sensors to the differential pressure sensors can enable environmentally-sensitive changes in n, impacting sensor output. Thus, when working with our two-port differential pressure sensors, we mitigate effects of thermal drift by creating a "dummy line" that connects to the second port of the differential pressure sensor (Fig. S6). The dummy line serves as a closed volume of tubing of approximately equal length to that used to connect the fluidic sensor to the first port of the differential pressure sensor. We wrap the dummy line around the tubing associated with the fluidic sensor in a braid-like fashion. This reduces any environmental influences on sensor output if we were to leave the second pressure sensor port exposed to the ambient atmosphere. The dummy line effectively equilibrates along with the fluidic sensor with which it is associated.

The differential pressure sensor connected to a fluidic sensor reports a nominal voltage of approximately 2.25 V when the sensor and dummy line have equilibrated. To demonstrate this, we conducted a 12 hour drift study in which measurements from the nine sensors of the cubic lattice were recorded at 1 Hz. We observed a mean voltage drift range of 0.11±0.04 V for the nine sensors, with the sensor displaying the most drift reporting an average voltage of 2.22±0.02 V (Fig. S7), indicating stable sensing.

Influence of Resin Viscoelasticity on Fluidic Sensor Response. Characterizing fluidic sensor responses via cyclic compression reveals that the photopolymer resins are viscoelastic: the maximum voltage during sensorized lattice compression to 10 or 20 mm decreases with increasing cycle count, indicating a strain-induced weakening response (Figs. S10 and S11). After approximately 70 cycles, the cylic voltage response's peaks begins to stabilize. We also compressed a sensorized BCC lattice for 10,000 cycles to 10mm at 1 mm/s (Figs. S12A,B). While we see a similar strain-induced weakening trend in this experiment, we also observe a creep response in the EPU resin when analyzing the load and compression response versus time (Fig. S12C). After thousands of cycles, we begin to observe the lattice not fully recovering from compression, and load is measured as 0 N with the lattice no longer pressing against the Instron platen. Other soft material based sensors exhibit dynamic, time-varying, hysteretic behaviors on account of their composition. For example, soft piezoresistive sensors show time-varying behaviors due to the dynamic nature of percolated conduction paths during deformation (21, 23). Our cyclic compression characterization experiments demonstrate that the viscoelastic behavior of our printing resins are responsible for any nonlinear behavior from the fluidic sensors. Otherwise, the fluidic sensing approach bypasses other time-varying responses, providing a reliable sensing approach compared to other soft matter-based sensing strategies.

Sensor Characterization in Straight sHSAs. We fabricated strain sHSAs with Full, Half, and Quarter sensors with diameters of 0.75, 1, 1.25, 1.5, and 1.75 mm to investigate how sensor diameter influence sensor response. We observed increasing sensitivity in the Full and Half sensors with increasing sensor diameter given that larger volumes produce larger pressure changes for a given deformation (Fig. S13). While these data suggest that working with 1750µm diameter sensors gives the greatest change in sensor voltage, these large diameter sensors are prone to failure during deformation given the thin shell of resin surrounding the fluidic sensors. For

this work, we print straight sHSAs having fluidic sensors with 1.5 mm diameters as they give sensitive sensor response and robust performance. Furthermore, we observed difficulties in consistently achieving reliable sensing in 0.75 mm-diameter sensors given the inconsistent success of clearly all excess resin from the channels (see *Materials and Methods*).

Prediction Results for sHSA Soft Robotic Platform: The results of the hyperparameter search are summarized in Tab. S1 and Fig. S19. The model with the lowest validation loss has a quaternion weight of 100, an initial learning rate of 0.001, 3 LSTM layers and 200 hidden and cell states. This model has a total of 856,007 trainable parameters and retraining it for 1000 epochs takes four hours on a single-GPU (Tesla P100, Nvidia Corporation). Its predictions on the test data exhibit an average position error of 3.2 mm and an average orientation error of 3.6 degrees. Considering the rest length of the sHSA platform of 120 mm and the range of motion in the recordings spanning 39.2 mm and 50.2 degrees, these errors are small. As in Fig. 4D, position and orientation errors are plotted over time for test sequences representative of good predictions (Fig. S21A,B) and test sequences representative of worse predictions (Fig. S21C,D). Component-wise predictions of the pose data are plotted against motion capture ground truth for the four aforementioned test sequences (Figs. S22, S23, S24, S25), and for the test sequence shown in Fig. 4D (Fig. S26).

The predictions for the test sequences, during which the platform moves continuously without stopping (such as in Fig. S22), are observed to be generally better than those in which the platform is held still for some time (such as Fig. S23, S24, S25, S26). One reason could be that the LSTM model learns from voltage changes, ΔV , rather than from absolute voltages values. This can produce larger errors when the platform is held still and the model happens to provide a wrong prediction for many time steps. This would explain the higher variance in quality of predictions for sequences with long holds (compare Fig. S23, S24, S25, S26). Another indication why this could be true is that even for predictions with larger errors, the timing of a pose change

is almost always predicted perfectly. This observation of pose prediction aligning so closely with pose change supports the claim that our fluidic sensors are robust compared to other forms of soft robotic sensors that yield slight time-delays in pose/kinematic predictions (21).

Supplementary Tables

Hyperparameter	Value	Minimum	Median	Maximum
Quaternion Weight	10	0.1498	0.3837	1.4822
	100	0.1440	0.4529	1.7351
	1000	0.1649	0.5299	2.3716
Learning Rate	0.001	0.1440	0.2280	0.9411
	0.005	0.1809	0.3571	0.7338
	0.01	0.3934	1.1064	2.3716
Hidden Layers	1	0.1809	0.4093	0.9411
	2	0.1505	0.4210	1.3825
	3	0.1440	0.4713	2.3716
Hidden Size	50	0.4368	0.6357	1.6430
	100	0.2211	0.3740	1.5879
	150	0.1661	0.2908	2.3716
	200	0.1440	0.2882	1.8824

Table 1: **Hyperparameter search results.** A grid search is performed over all combinations of values shown for each hyperparameter in the Value column. For each specific combination of hyperparameters, the validation loss averaged over three trials is recorded. For a certain value of one hyperparameter, the marginal distribution of validation losses is computed over all values of all other hyperparameters. Minimum, median, and maximum of this marginal distribution are tabulated. I.e., the first row means all 36 combinations² with a quaternion weight of 10 result in a median validation loss of 0.3837. The minimal validation loss for each hyperparameter is shown in bold.

 $^{^23 \}times 3 \times 4 = 36$ since there are three possible values for learning rate (0.001, 0.005, 0.01), three possible values for hidden layers (1,2,3), and four possible values for hidden size (50, 100, 150, 200).

Supplementary Figures

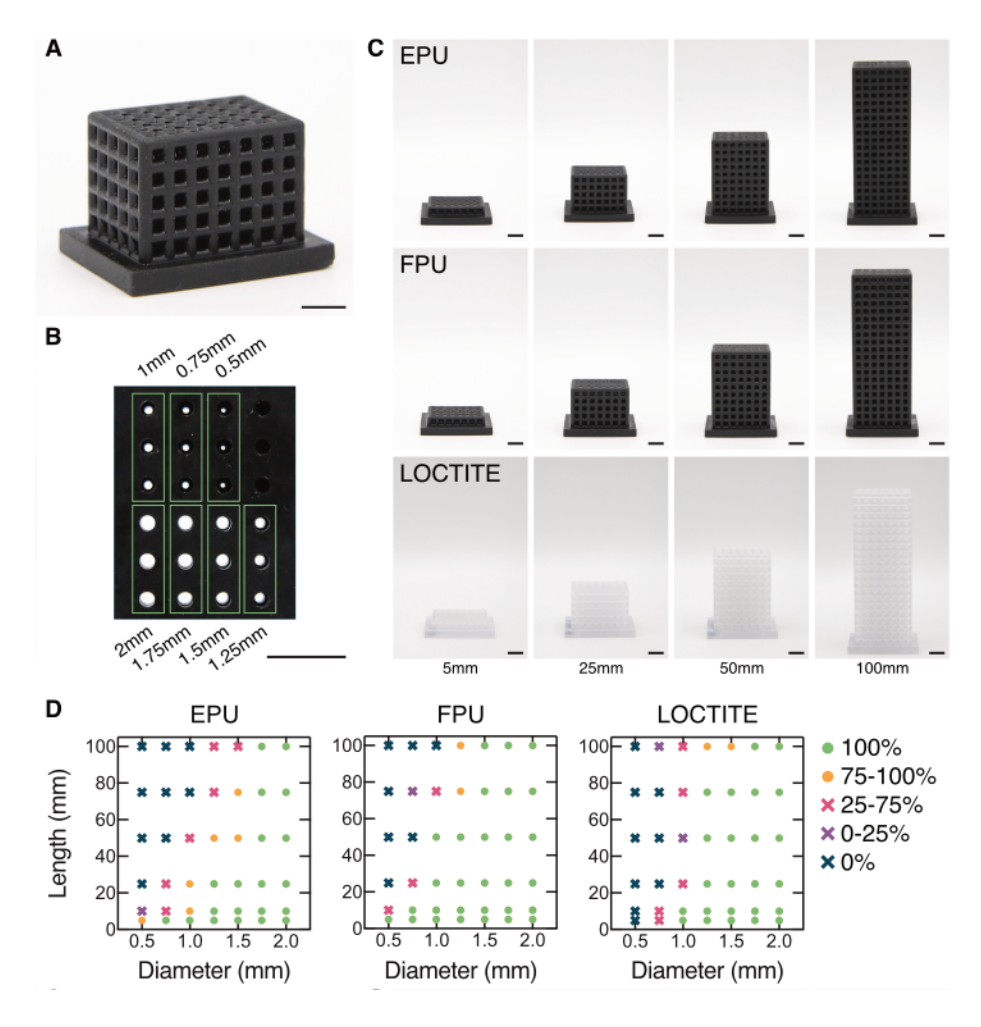


Figure 5: **Fluidic sensor fabricability.** (A) A photograph of an example lattice used to characterize fluidic sensor fabricability (EPU, length of 25 mm). (B) Each test lattice has 21 channels embedded along its length. Three channels of varying diameter (0.5 to 2 mm) are clustered as indicated by the green rectangles in the photograph of the underside of a test lattice. The photograph shows open channels in a test lattice with a length of 5mm as viewed from the base, looking down the length of the fluidic channels. (C) Photographs are shown for EPU (top), FPU (middle), and LOCTITE (bottom) test lattices of length 5, 25, 50, and 100 mm. (D) Success of fluidic sensor fabrication (for n = 12 sensors per geometry) is provided for EPU (left), FPU (middle), and LOCTITE (right) test lattices for the various channel lengths and diameters screened. (Scale bars represent 10 mm.)

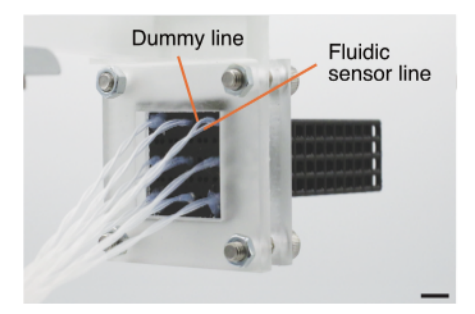


Figure 6: **Mitigating thermal drift with dummy lines.** The photograph indicates the fluidic sensor line and dummy line for the top left sensor of the cubic lattice. All nine sensors show the braid-like wrapping of dummy lines around the main tubing connecting the fluidic sensor with the differential pressure sensor. (Scale bar represents 10 mm.)

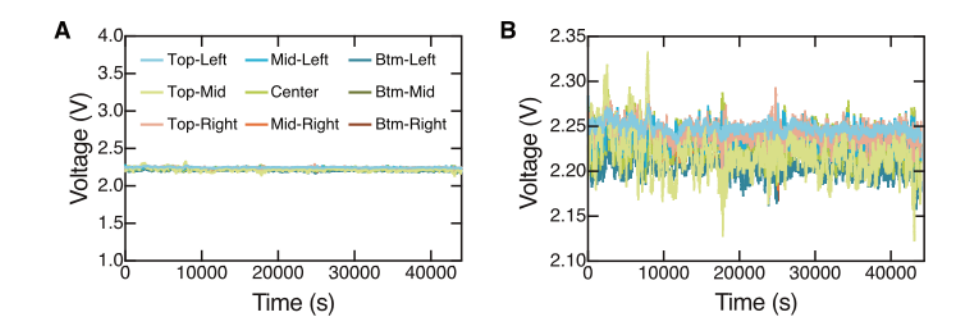


Figure 7: **Thermal drift of sensors.** (A) The voltages for the nine sensors of the cubic lattice are shown over a 12 hour time period and plotted over the sensing range of the differential pressure sensor (1 to 4 V). (B) A closer view of the data reveals that sensors generally remain stable over the 12-hour period.

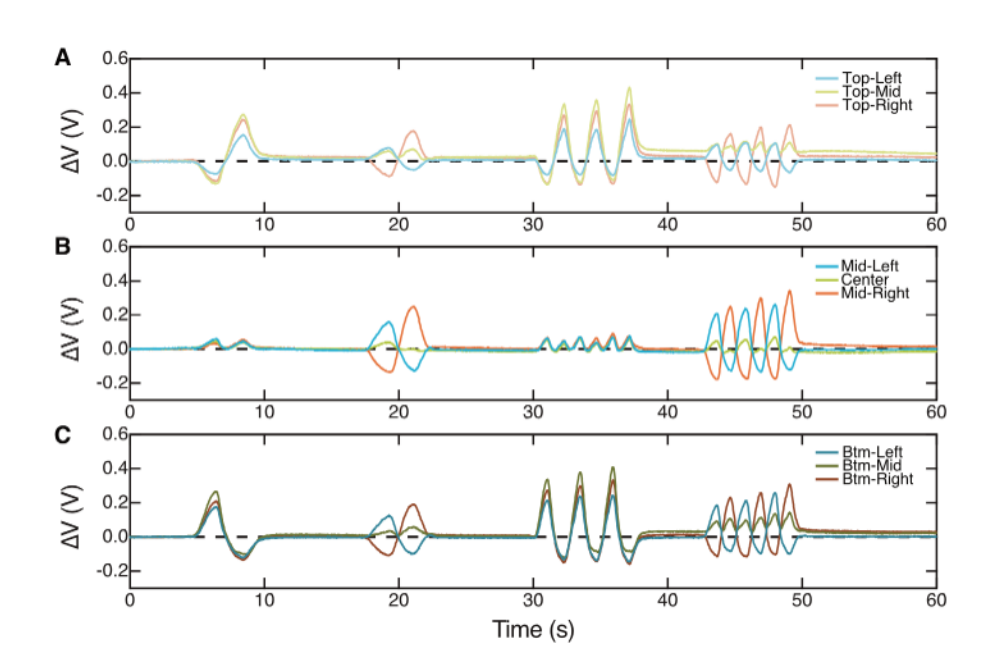


Figure 8: **Detail of sensor response during cubic lattice bending.** Detailed plot of voltage change, ΔV , over time from all sensors during the manual bending experiment shown in SI Video 2 and Figure 1F separated into responses for the three (A) Top, (B) Middle, and (C) Bottom (Btm) fluidic sensors.

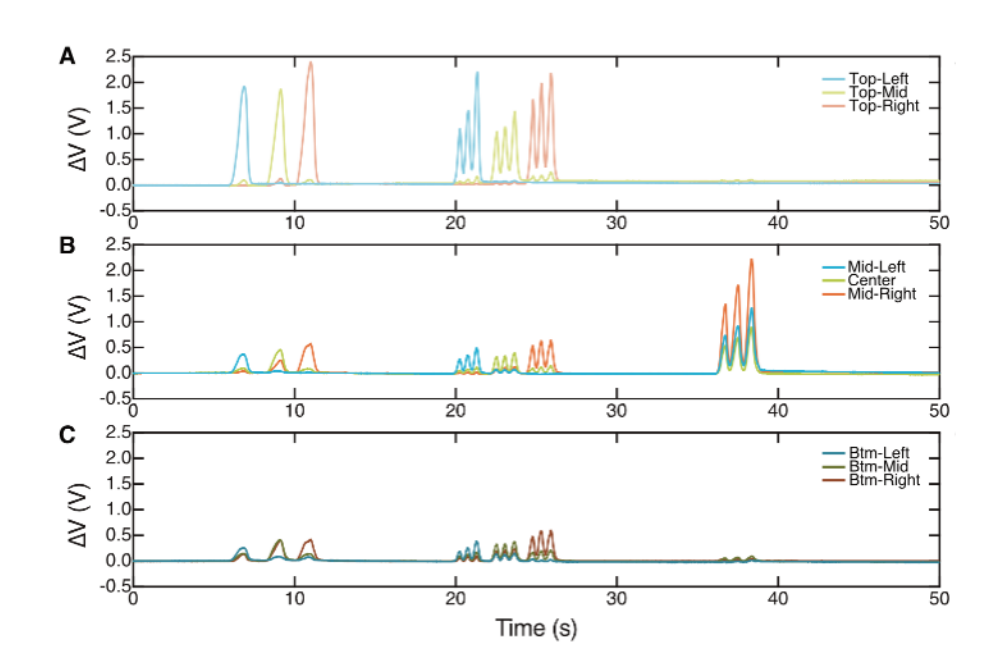


Figure 9: **Detail of sensor response during cubic lattice pressing.** Detailed plot of voltage change, ΔV , over time from all sensors during the manual tactile, pressing experiment shown in SI Video 2 and Figure 1H separated into responses for the three (A) Top, (B) Middle, and (C) Bottom (Btm) fluidic sensors.

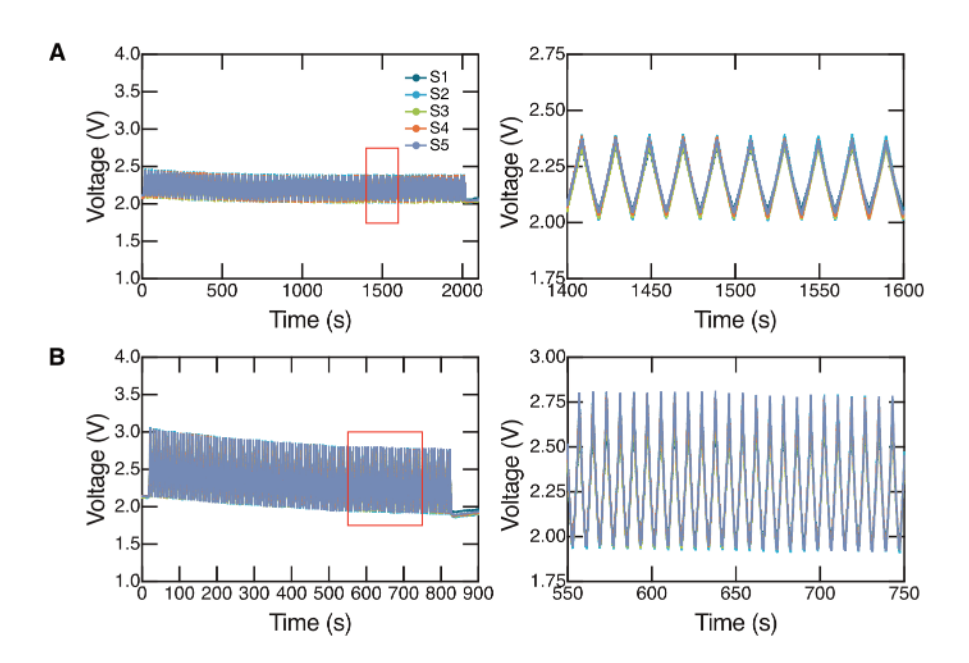


Figure 10: Cyclic compression of sensorized BCC lattices. Plots of voltage versus time for the five fluidic sensors (S1 through S5) of the sensorized BCC lattice during 100 cyclic compressions (A) to 10mm at 1 mm/s and (B) to 20mm at 5 mm/s. Plots in the right column are insets of left column plots indicated by the red rectangle.

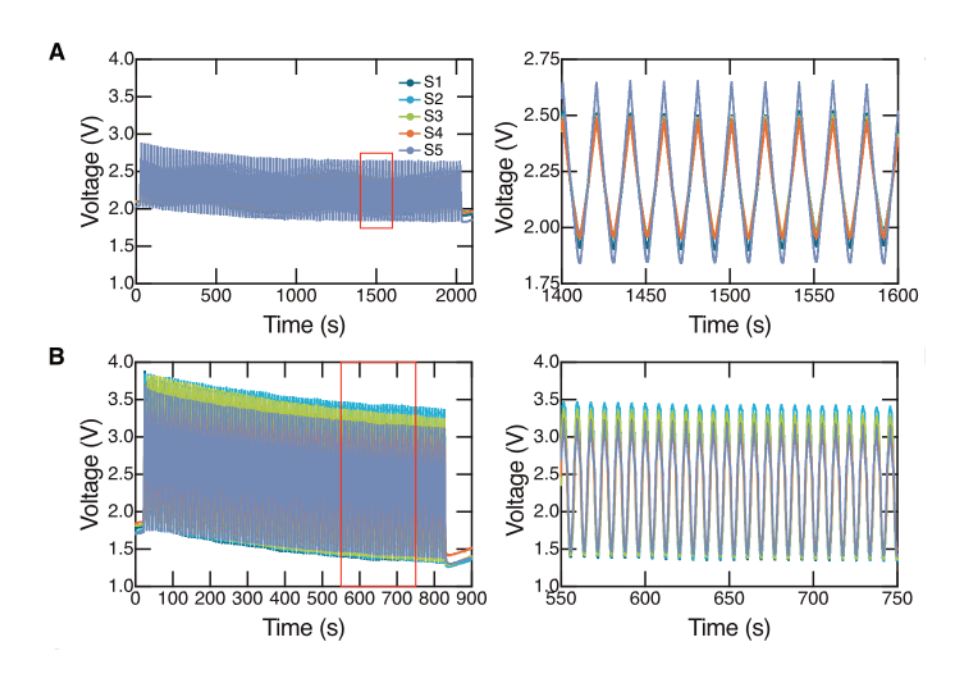


Figure 11: Cyclic compression of sensorized Octahedral lattice. Plots of voltage versus time for the five fluidic sensors (S1 through S5) of the sensorized Octahedral lattice during 100 cyclic compressions (A) to 10mm at 1 mm/s and (B) to 20mm at 5 mm/s. Plots in the right column are insets of left column plots indicated by the red rectangle.

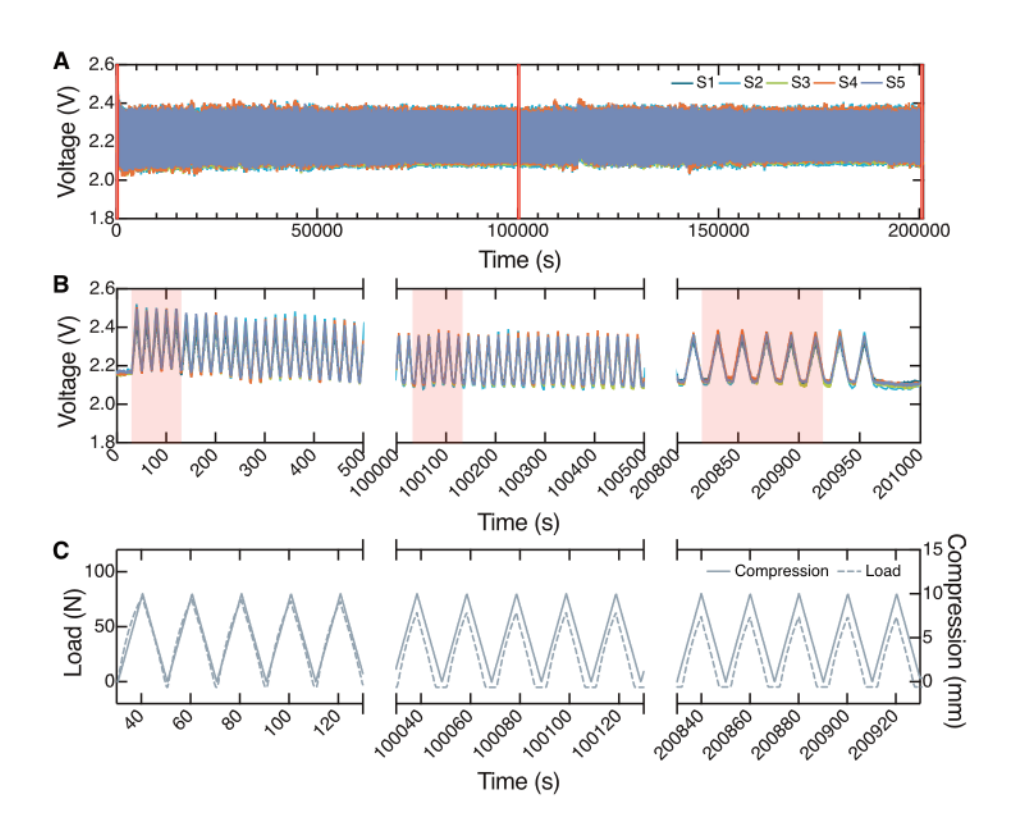


Figure 12: Sensor characterization during 10,000 cycles of compression. (A) A plot of voltage versus time for the five sensors (S1 through S5) of the sensorized BCC lattice during 10,000 cycles of compression to 10mm at 1 mm/s. (B) The three voltage versus time plots correspond to the three insets marked by the three red rectangles in A. (C) Plots of load (dashed line) and compression (solid line) versus time for the three regions of B marked by the shaded red rectangles.

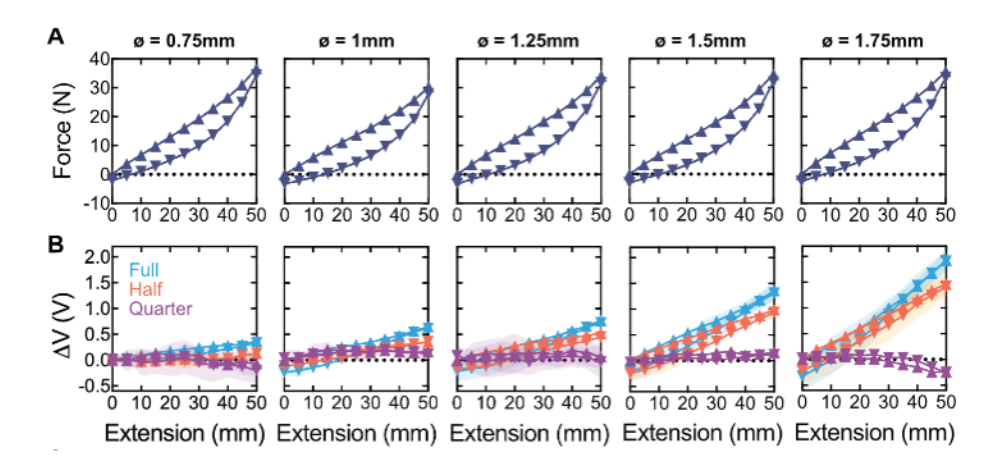


Figure 13: Characterization of sHSA Full, Half, and Quarter Sensors of Varying Diameter. (A) Plots of extension force and (B) voltage change, ΔV , for Full, Half, and Quarter Sensors versus extension are provided. Columns of plots correspond to data for sHSAs with Full, Half, and Quarter sensors with diameters of 0.75mm, 1mm, 1.25mm, 1.5mm, and 1.75mm.

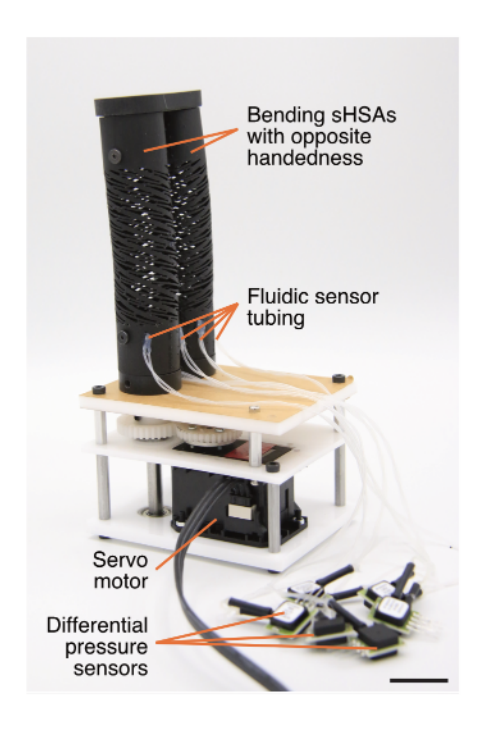


Figure 14: **sHSA Bending Actuator.** Photograph of the sHSA bending actuator comprised of a 2x1 grid of sHSAs with opposite handedness. Each sHSA has 1.0mm diameter "3/4", "1/2", and "1/4" sensors.

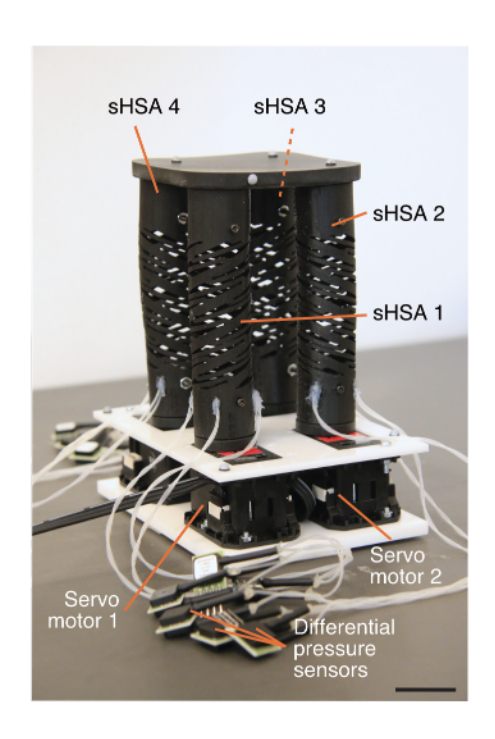


Figure 15: **sHSA platform.** Photograph of the sHSA platform comprised of a 2x2 grid of sHSAs with alternating handedness. Each sHSA has 1.5mm diameter "Full", "Half", and "Quarter" sensors.

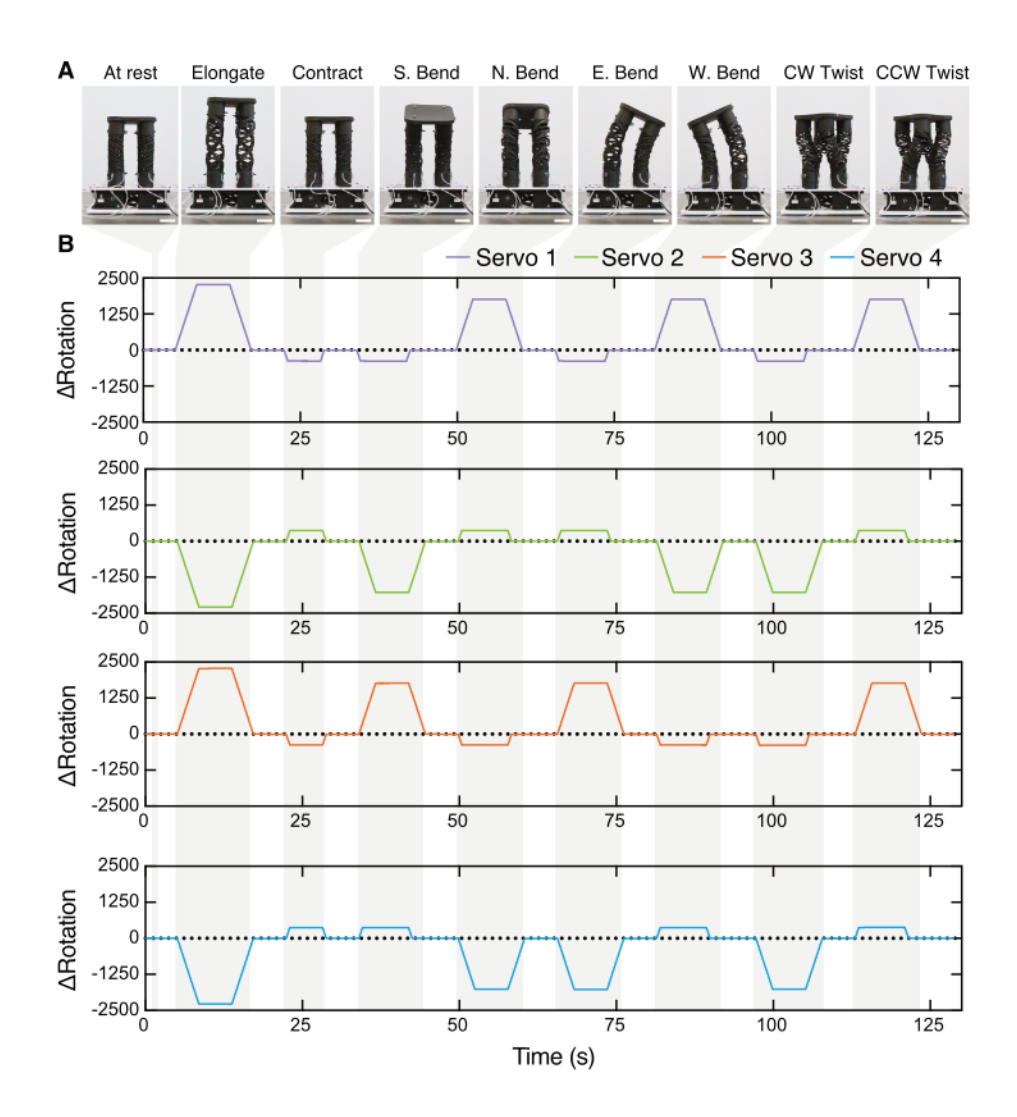


Figure 16: **Servo rotations for sHSA platform.** The data corresponds to Figure 4A-B in the main manuscript, with (A) photographs of the same platform poses provided. (B) The corresponding change of servo rotation (Δ Rotation) for Servos 1 through 4, which drive sHSAs 1 through 4, respectively, are provided as a function of time. Scales bars represent 25 mm.

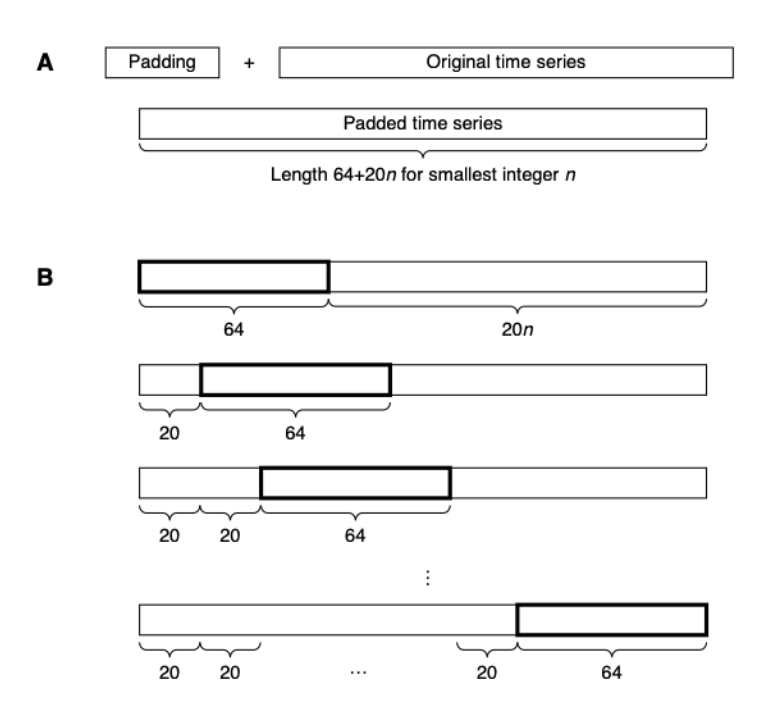


Figure 17: **Preprocessing of training data.** Sequences of length 64 are extracted from each of the 180 experiments. (A) Each of the original time series is padded such that the new length equals 64+20n for the smallest integer n. The data with which the time series is padded is the first data point of that sequence, which consists of zero pressures for the inputs and the initial pose for the outputs. (B) Extracting n data sequences of length 64 by sliding a window (marked in bold) over the padded time series with a stride of 20. This method simultaneous augments the data as four consecutive length-64 sequences contain overlapping time points.

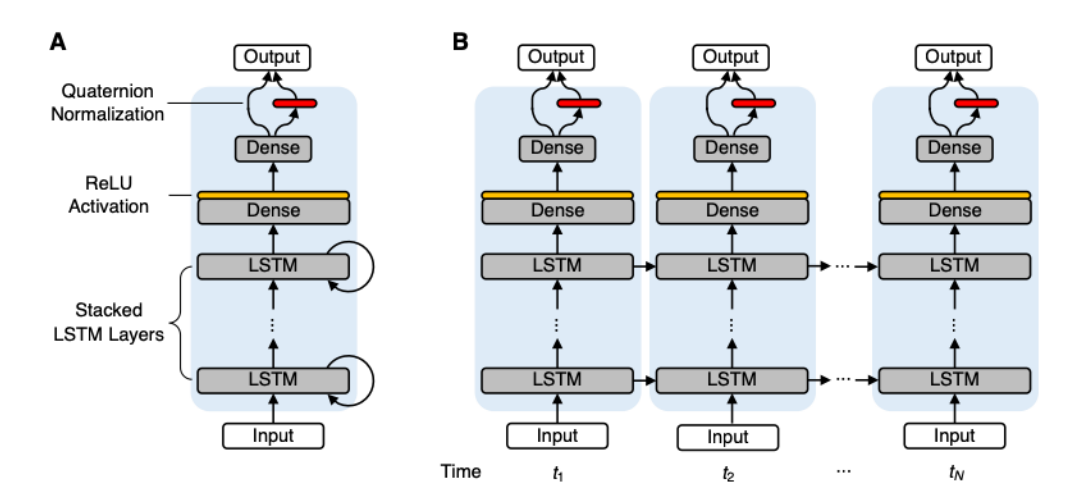


Figure 18: **LSTM** for proprioceptive sensing in sHSA platform. (A) Model architecture. The 12-dimensional input is passed through stacked LSTM layers, where number of layers and size of their hidden and cell states are tunable hyperparameters. A dense layer with equal size is followed by ReLU activation and another dense layer that outputs a 7-dimensional vector. This vector is passed through a layer that normalizes the four values corresponding to the quaternion outputs. Dropout with probability 0.2 is applied to the first dense layer and each LSTM layer (not shown). (B) Forward pass unrolled through time for input sequence of length *N*.

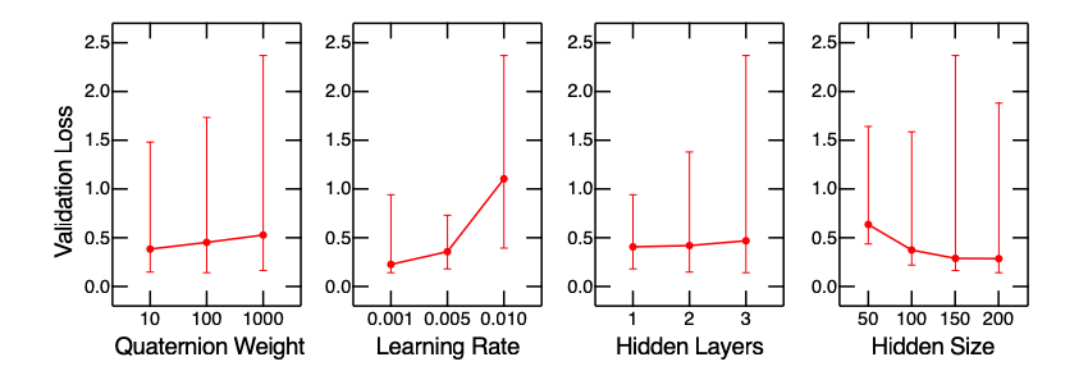


Figure 19: **Hyperparameter search results.** A grid search is performed over all combinations of the displayed values for each hyperparameter. The validation loss is averaged over three runs for each combination to account for randomness. The plots show median validation loss and range (error bars) of the marginal distribution over all other hyperparameters. See Tab. S1 for numerical values and further explanation.

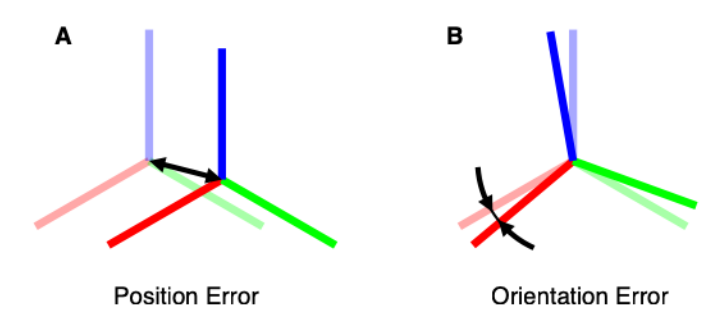


Figure 20: Error metrics. Schematic to illustrate the error metrics that are used to evaluate the final model perfomance on the test data. (A) The position error is defined as the distance between the origins of the predicted pose (opaque RGB coordinate axes) and the ground truth pose (transparent RGB coordinate axes). (B) The orientation error is defined as the relative rotation between the poses.

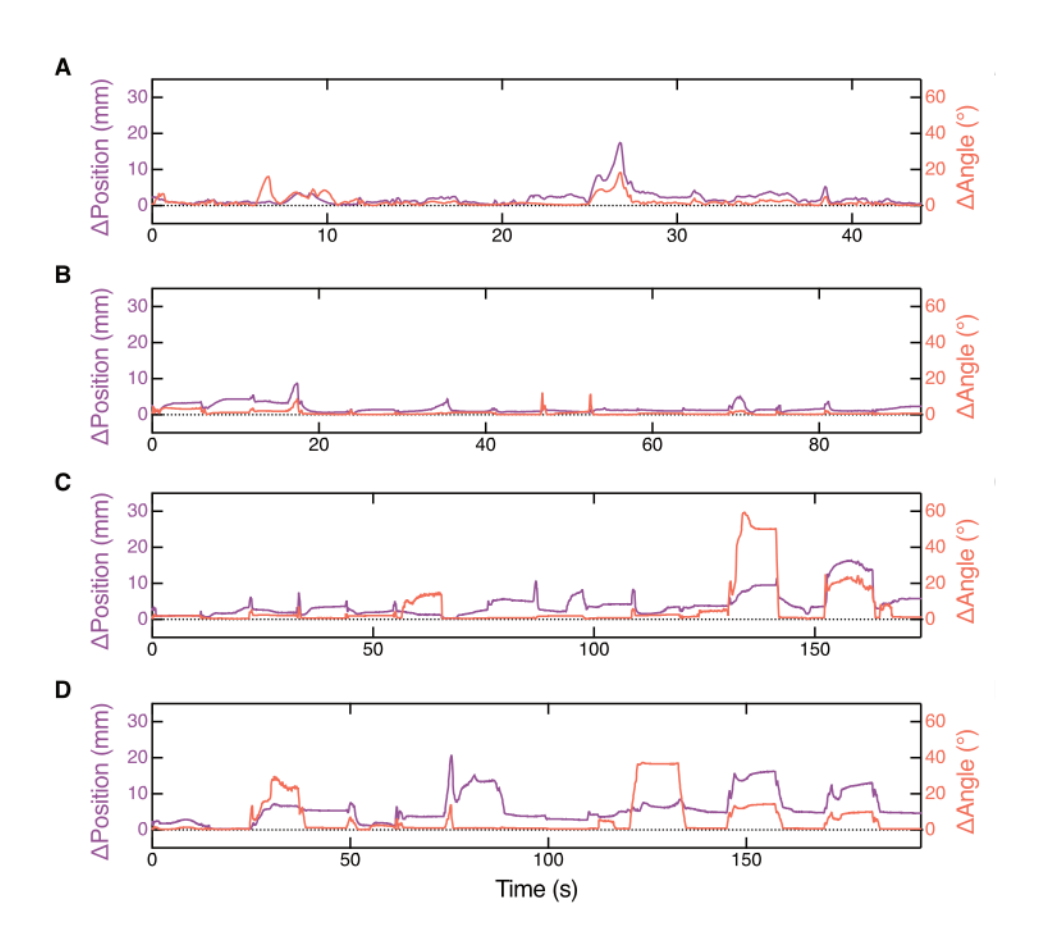


Figure 21: **Representative prediction errors.** Position (Δ Position) and orientation (Δ Angle) error over time for a set of representative test sequences giving better (A,B) and worse (B,C) predictions. (A) Test sequence 1 has an average position error of 2.1 mm and an average orientation error of 2.3 degrees. (B) Test sequence 2 has an average position error of 1.8 mm and an average orientation error of 1.0 degrees. (C) Test sequence 3 has an average position error of 4.1 mm and an average orientation error of 6.3 degrees. (D) Test sequence 4 has an average position error of 5.9 mm and an average orientation error of 5.9 degrees.

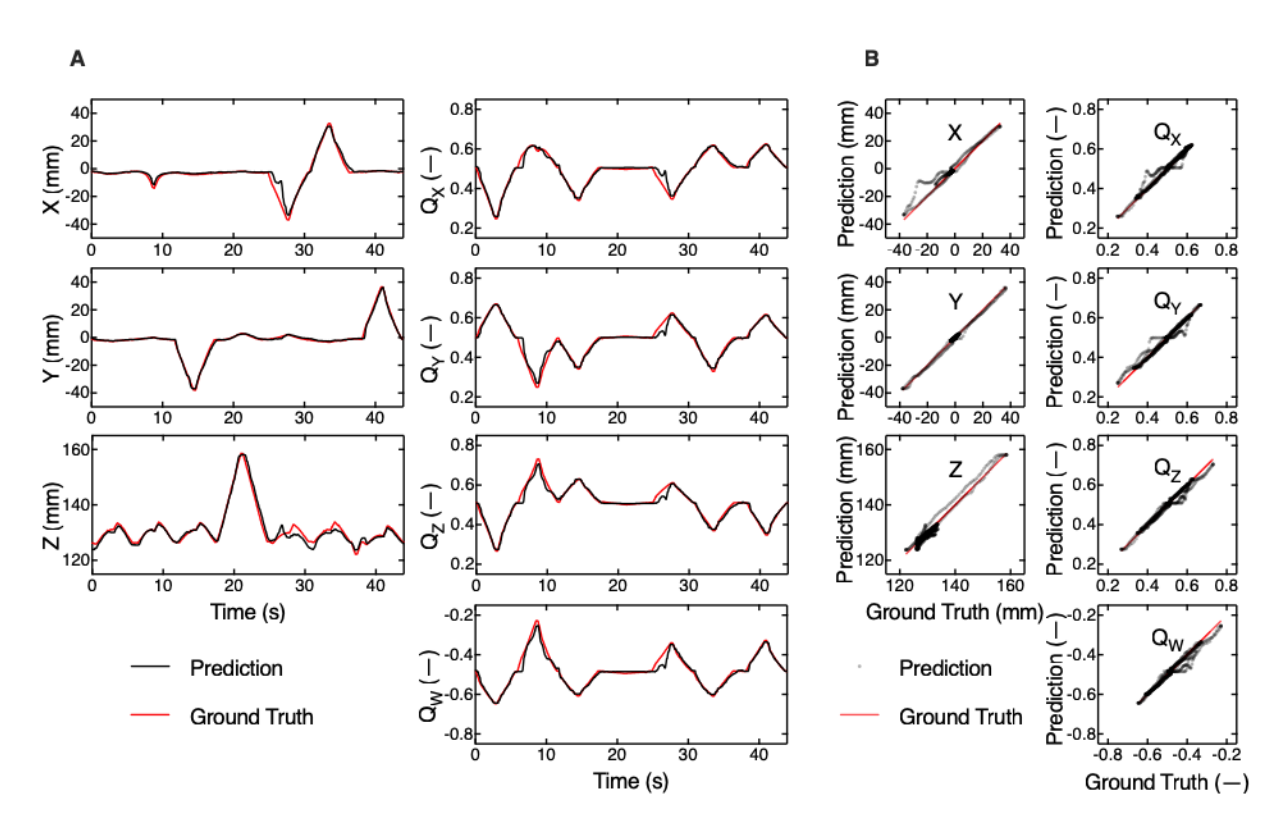


Figure 22: Component-wise predictions for test sequence 1. Prediction and motion capture ground truth for a test sequence that is representative of a typical good prediction, broken down into position (X,Y,Z) and quaternion (Q_X,Q_Y,Q_Z,Q_W) components. (A) Prediction (black) and ground truth (red) over time. (B) Prediction (grey dots) over ground truth (red line).

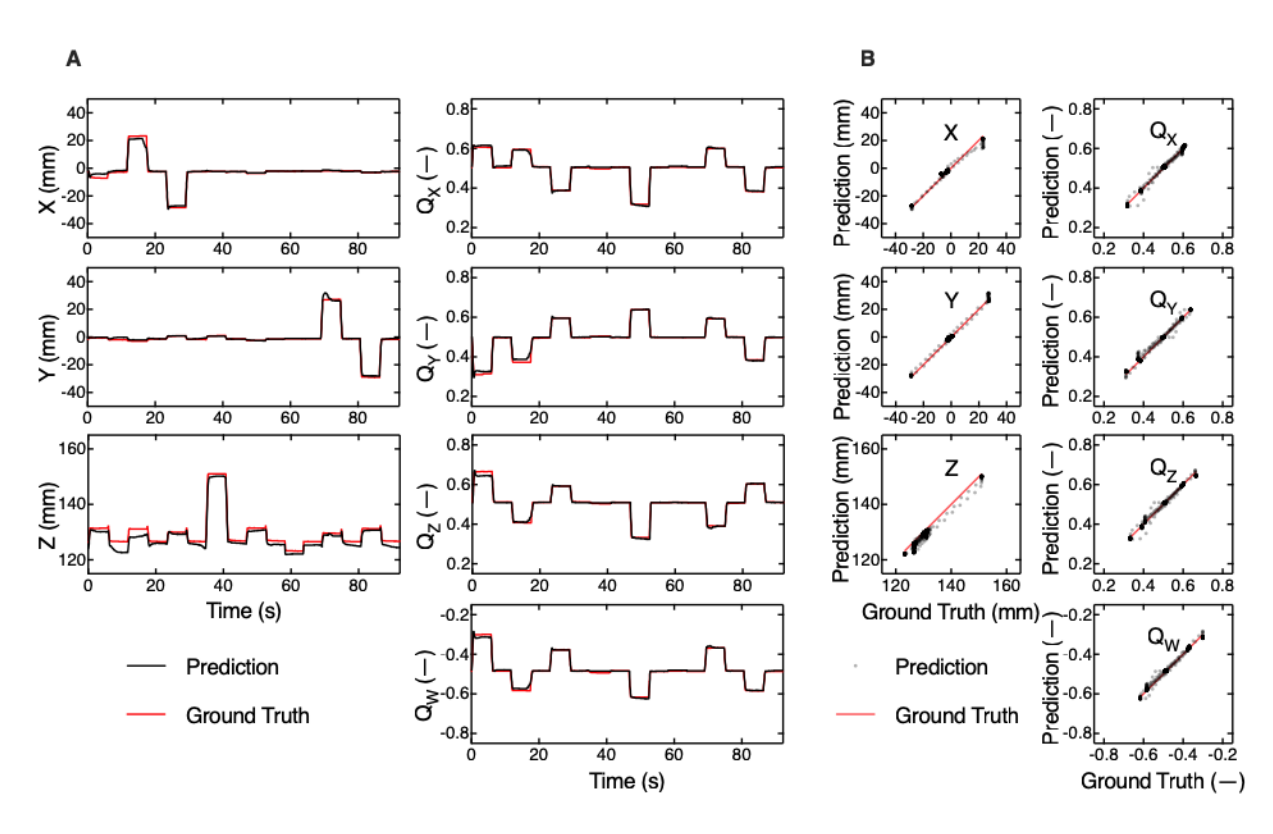


Figure 23: Component-wise predictions for test sequence 2. Prediction and motion capture ground truth for a test sequence that is representative of a typical good prediction, broken down into position (X,Y,Z) and quaternion (Q_X,Q_Y,Q_Z,Q_W) components. (A) Prediction (black) and ground truth (red) over time. (B) Prediction (grey dots) over ground truth (red line).

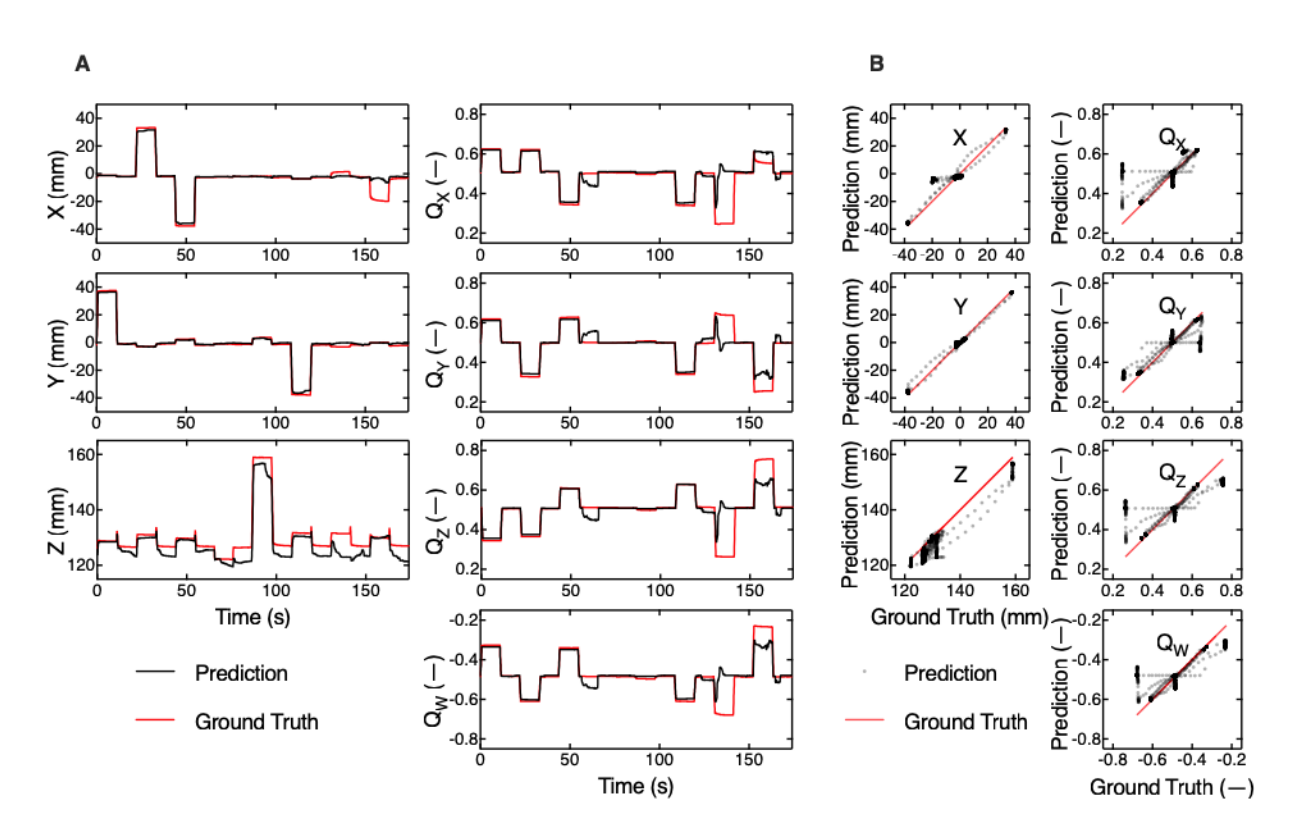


Figure 24: Component-wise predictions for test sequence 3. Prediction and motion capture ground truth for a test sequence that is representative of a worse prediction, broken down into position (X,Y,Z) and quaternion (Q_X,Q_Y,Q_Z,Q_W) components. (A) Prediction (black) and ground truth (red) over time. (B) Prediction (grey dots) over ground truth (red line).

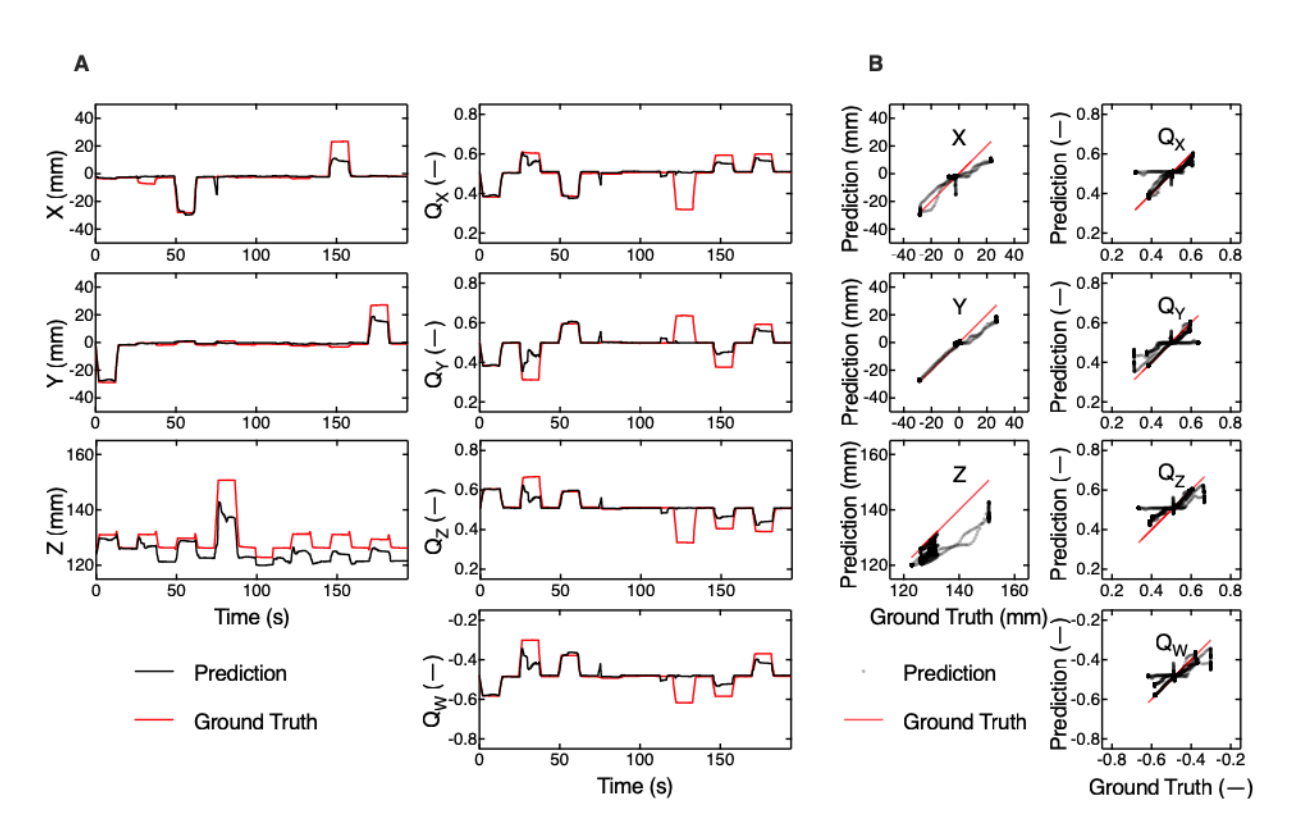


Figure 25: Component-wise predictions for test sequence 4. Prediction and motion capture ground truth for a test sequence that is representative of a worse prediction, broken down into position (X,Y,Z) and quaternion (Q_X,Q_Y,Q_Z,Q_W) components. (A) Prediction (black) and ground truth (red) over time. (B) Prediction (grey dots) over ground truth (red line).

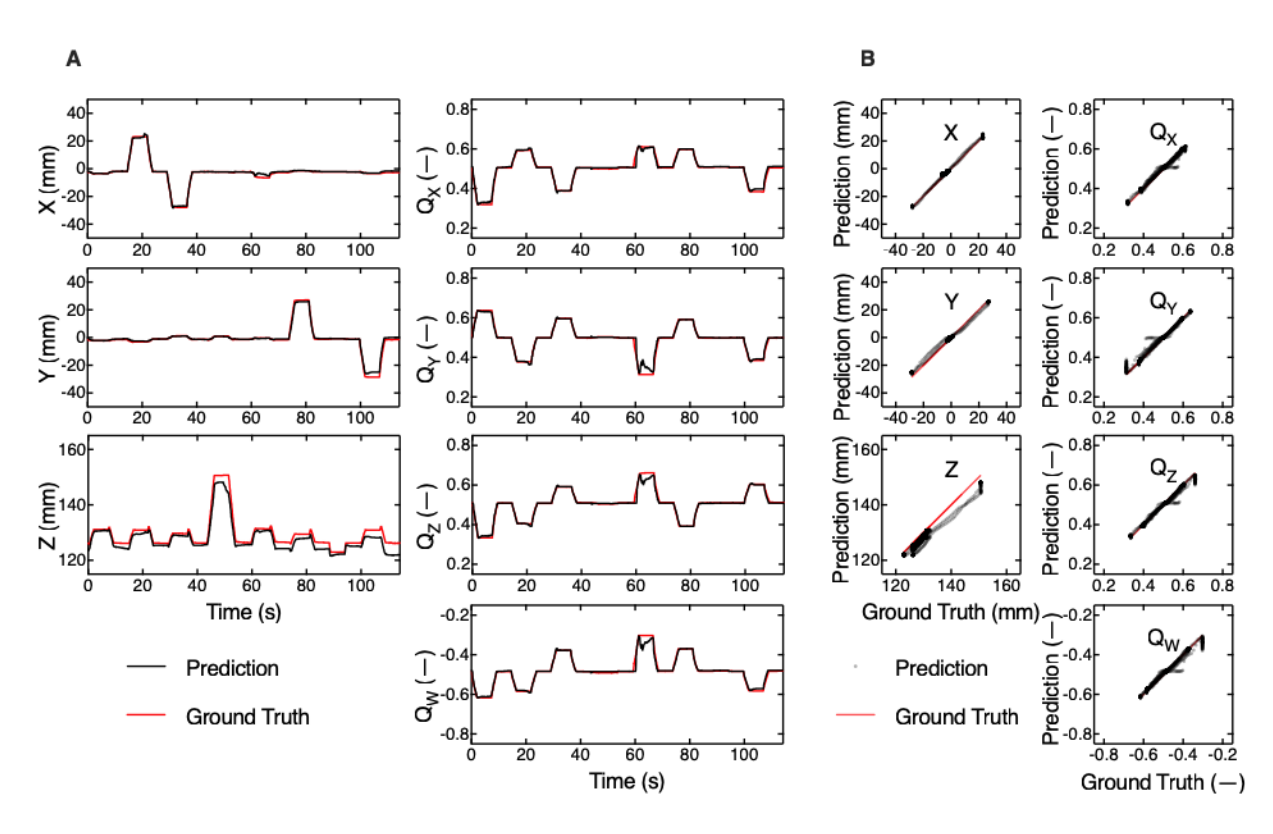


Figure 26: Component-wise predictions for test sequence shown in Fig. 4. Prediction and motion capture ground truth for the test sequence shown in Fig. 4, broken down into position (X,Y,Z) and quaternion (Q_X,Q_Y,Q_Z,Q_W) components. (A) Prediction (black) and ground truth (red) over time. (B) Prediction (grey dots) over ground truth (red line).

NOTE ABOUT FIGURES (Fig. 1). Please do not use figure environments to set up your figures in the final (post-peer-review) draft, do not include graphics in your source code, and do not cite figures in the text using LATEX \ref commands. Instead, simply refer to the figure numbers in the text per *Science* style, and include the list of captions at the end of the document, coded as ordinary paragraphs as shown in the scifile.tex template file. Your actual figure files should be submitted separately.